JOURNAL OF
CIVIL ENGINEERING
PUBLICATION OF THE NIGERIAN INSTITUTION OF CIVIL ENGINEERS
(A Division of the Nigeria Society of Engineers)
...Sustaining the World's Infrastructure

VOL. 15 NO. 1/ ISSN 2811 -2806 / DECEMBER,2022

CONTENTS

VISION

Nigerian Institution of Civil Engineers shall be a world renowned body, whichwill be a pride to all Civil Engineers in Nigeria.

MISSION STATEMENT

To make unique contribution to the development process of the country by constituting itself such that it will be a reservior of Civil Engineers with specialized knowledge, experience and skill, constantly updated through the highest standard of continuing professional development programmes.

To establish and maintain standards and codes for the practice of Civil Engineering in nigeria.

To be constantly in touch with the Government at all levels, for necessary inputs and contributions to policies and matter affecting members and the development of the profession.

NATIONAL CHAIRMAN'S CORNER

Engr. Dr. Jang C. Tanko,
FNSE,FINCE
National Chairman

Over the years, Civil Engineering has proven to be the indisputable mother of all engineering professions and by far the broadest of all engineering fields. It focuses in the infrastructure of the entire universe including but not limited to Waterworks, Sewers, Dams, Power Plant, Transmission Towers/Lines, Railroads, Highways, Bridges, Tunnels, Irrigation Canals, River Navigation, Shipping's Canals, Traffic Control, Mass Transit, Airport Runways, Terminals, Industrial Plants, Buildings, skyscrapers etc. Among the important sub divisions of the field are construction Engineering, Geotechnic Engineering, Hydraulic Engineering and Coastal/Oceanic Engineering.

Civil Engineers build the world's infrastructure. By so doing, they quietly but surely shape the history of nation around the world! Life is just one unbearable experience without the numerous contributions of Civil Engineers to the public's health safety and standard of living. Only by exploring Civil Engineers' influence in shaping today's world can we creatively envision the progress of our tomorrow.

It is paramount to me as the National Chairman of NICE at this point of our National Development, that we build an Institution that will continuously strife to make an endearing impact to the growth and development of our nation. It is in this regards that I want to encourage every member of our Institution to get a copy of this journal, which is an integral instrument of professional development to the individual Civil Engineer, and also help to enhance the projection of our innovative ideals to compete both locally and internationally. Finally, I implore all Civil Engineers to avail themselves of the opportunities presented through the publication of this quarterly Civil Engineering Journal, to come up with technical papers that will improve and promote the practice of Civil Engineering in Nigeria in a positive perspective to the world.

Thank You.

TECHNICAL COMMITTEE CHAIRMAN'S COMMENT

I wish to present a new edition of the Journal of Civil Engineering published by the Nigerian Institution of Civil Engineers. This Journal is conceived to disseminate original contributions from the Academia as well as the Public and Private Sector Practitioners of the profession of Civil Engineering. This year's edition contains scholarly interventions that permeate several branches of the Civil Engineering family profession such as Structural, Geotechnical, Water Resources and Environment, Highway and Transportation Engineering. It is with a great sense of honour and responsibility that I invite you to read and enjoy this new edition.

Engr. Dr. Ezekiel B. Coker, FNSE, FNICE
Chairman Sub-Technical Committee

2022 NATIONAL EXECUTIVE COMMITTE

ENGR. DR. JANG C. TANKO,FNSE,FNICE
NATIONAL CHAIRMAN

ENGR. VIRGILUS C. EZUGU,FNSE,FNICE
DEPUTY NATIONAL CHAIRMAN

ENGR. SONNY E. ALLI, FNICE
NATIONAL VICE CHAIRMAN

ENGR. OLUMOH SHARAFADEEN A.,FNSE FNICE
NATIONAL VICE CHAIRMAN

ENGR. Tokunbo Ajanaku, FNSE FNICE
NATIONAL VICE CHAIRMAN

ENGR. Dawood A, Kelani,FNICE
Ex-Officio

ENGR. Bukar Kadal, FNICE
Ex-Officio

ENGR. Sir Alexander I. Onichabor,FNICE
Ex-Officio

Engr. Mrs. Aishatu A. Umar,FNSE, FNICE
Former Immediate Past. National Chairman

ENGR. Boaz T. David, FNSE, FINCE
Ag- Executive Secretary

EFFECTIVE COMPUTATION OF FENESTRATION REQUIREMENTS IN BUILDING ENVELOPES

EDOKPOLO, E. L.O
DEPARTMENT OF ARCHITECTURE,
AMBROSE ALLI UNIVERSITY, EKPOMA, EDO STATE

Abstract

The aim of this study was to appraise fenestration in buildings and determine appropriate methods of computation of effectiveness. The following objectives were to: identify major factors that affect fenestration in building envelopes; determine the extent of impact of each of these factors that affect fenestration and recommend appropriate computational methods for effective fenestration using these factors. The study employed a survey technique in eliciting information on the subject matter. A total of one hundred and fifty professionals were interviewed and questionnaires administered on them and retrieved by the researcher. A 4- point Likert scale was adopted with a maximum score of 4.0 and a criterion mean score of 2.50. The findings of these focus group interviews, questionnaires and personal observations were correlated with existing mathematical relationships of the major factors that affect fenestration and recommendations were made. The study found out that the major factors that affect fenestration in building envelopes are, in accordance with their ranks: thermal conductance/ u-values of components of the envelope, TC/U-V (1); solar exposure, SE (2); total area of glazing elements, TAGE (3); solar heat gain, SHGC (4); orientation of glazed elements, OGE (5); climatic zone, CLZ (6); total floor area, FLA (7); projections and shades, P & S (8). The issue of fenestration is as old as the concept of building, itself. Thermal comfort in buildings is paramount in design and construction considerations. At the design stage, effective fenestration is affected by: thermal conductance/ u-values of components of the envelope; solar exposure; total area of glazing elements; solar heat gain; orientation of glazed elements; climatic zone; total floor area; projections and shades. A methodical multi-variate approach was recommended for effective fenestration in building envelopes.

1.0 Introduction

1.1 Background to the Study

Building envelope constitutes the limit between the interior and exterior conditions and its correct selection is one of the most effective ways to minimize the energy consumption related to interior thermal comfort (Attia et al., 2013). When the building envelope is conceived as a barrier that protects from the exterior conditions, the thermal transmittance (U value) is its most relevant characteristic. Building codes, as well as the voluntary certifications, are becoming more demanding in terms of the thermal transmittance of the envelope. There has been some discussion as to whether the high standards of insulation may or may not lead to increased loads. To enhance the overall thermal comfort of building envelopes, fenestration is necessary (Barry, 2011). **Fenestration** refers to the openings in the building envelope, including the installation of windows, doors, and skylights. Fenestration means the arrangement of windows,

doors and other openings in a building. A well-designed structure has a balanced arrangement and proportion of fenestration to facilitate optimum space and daylight. The inclusion of windows and other openings in the home are necessary as they improve the overall environment inside the home (Corgnati et al, 2011). However, they do work to break the seal of the home, providing possible places for air, water, and cold air to enter the home. Thus, the number of openings included in a home must be taken into account, as well as the quality of the materials used to create these openings along with the placement (Attia et al., 2013). This is a factor of natural ventilation which is a **major way of improving energy efficiency in buildings.** Natural ventilation via fenestration is the intentional passive flow of sub aerial air into a building through openings (such as louvers, doors, and windows). It can also be used for purposes of thermal comfort or dehumidification. The correct introduction of ambient air will help to achieve desired indoor comfort levels although this varies from individual to individual (Afon, 2000). Natural ventilation via fenestration does not require mechanical systems to move sub aerial air. It relies entirely on passive physical phenomena, such as diffusion, wind pressure, or the stack effect. It harnesses naturally available forces to supply and remove air in an enclosed space (Edokpolo, 2020). Wind driven ventilation relies upon effective fenestration and the force of the prevailing wind to pull and push air through the enclosed space as well as through breaches in the building's envelope (Barry, 2011). Almost all historic buildings were ventilated naturally using effective fenestration. The technique was generally abandoned in larger US buildings during the late 20th century as the use of air conditioning became more widespread.

However, with the advent of advanced Building Energy Modeling (BEM) software, improved Building Automation Systems (BAS), Leadership in Energy and Environmental Design (LEED) design requirements, and improved window manufacturing techniques; natural ventilation with specific fenestration characteristics has made a resurgence in commercial buildings both locally and globally (Corgnati et al, 2011). Fenestration also refers to products classified as either vertical fenestration or skylights and sloped glazing, installed in such a manner as to preserve the weather resistant barrier of the wall or roof in which they are installed. Fenestration includes products with glass or other transparent or translucent materials. Vertical fenestration includes windows that are fixed or movable, opaque doors, glazed doors, glazed block, and combination opaque and glazed doors installed in a wall at less than 15 degrees from vertical; Skylights and Sloped Glazing such as Glass or other transparent or translucent glazing material installed at a slope of 15 degrees (0.26 rad) or more from vertical (Attia et al., 2013). Unit skylights, tubular daylighting devices and glazing materials in solariums, sunrooms, roofs and sloped walls are included in this definition. These definitions clarify that fenestration consists of vertical glazing, skylights and sloped glazing, and preserves the weather-resistant barrier of the building envelope component it is placed in. It also clarifies that tubular daylighting devices are to be treated as fenestration and, therefore, must be installed in such a manner as to preserve the weather resistance of the roof in which they are installed. Finally, they establish the angle at which fenestration goes from being vertical to sloped glazing as 15 degrees from vertical (Ruth, 2016).

1.2 Statement of Problem

The reason for this study is mainly justified by the rising rate of thermal discomfort reported annually by building occupants which has been making occupants of very beautiful homes to find thermal comfort outside their homes. Secondly, there is also a tremendous rise in cost of fossil fuels. Thirdly, there is the realization that the conventional sources of energy for mechanical cooling, heating and artificial lighting are major contributors to the increase in greenhouse gas emissions that, in turn cause global warming (International Panel on Climate Change, IPCC, 2013). According to the Intergovernmental Panel on Climate Change (IPCC, 2014) in 2010 the building sector accounts for about 32% of the global energy consumption, 19% of energy-related CO2 emissions, and 51% of the global electricity consumption. In that same year only about 8% of the world's energy was consumed by commercial buildings, whereas residential buildings were responsible for 24% of the total final energy consumption (IPCC, 2014). Most of the pollutions are indirect emissions from electricity use in buildings, thus, the actual emission values mainly depends on electricity production and varies in different regions around the world.

In Western Europe and North America, residential buildings accounted for about 67% and 56% of the end energy use in buildings, in North Africa and Sub Saharan Africa the housing sector accounted for about 79% and 97% of the energy use in buildings (IPCC, 2014). Thus, switching to renewable energy sources or reducing the energy use in residential buildings in Africa is crucial for limiting greenhouse gas emissions in the region and mitigating global warming. Nowadays it is very well known that, one of the most effective ways for reducing energy use in buildings, including residential buildings, is by incorporating passive design approaches at the early stages of the design process (Attia et al., 2013). This paper focuses on the use of effective fenestration as a tool for passive design for improvements to thermal and visual conditions in buildings without requiring mechanical heating, cooling and/or artificial lighting.

1.3 Aim and Objectives of the Study

The aim of this paper was to appraise fenestration in buildings and determine appropriate methods of computation of effectiveness. The following objectives were to:

a. Identify major factors that affect fenestration in building envelopes;
b. Determine the extent of impact of each of these factors that affect fenestration and
c. Recommend appropriate computational methods for effective fenestration using these factors.

1.0 Application of Effective Fenestration in Buildings

Modern homes and commercial spaces are continuously experimenting with ways of using fenestration to ensure light transmittance and passive cross-ventilation (Attia et al., 2013). Many commercial spaces such as malls, offices and hotels today use fenestration tricks for energy efficiency and reduced costs. Fenestration plays a major role in setting the interior atmosphere and defining the external appearance of a structure (Barry, 2011).

The following are a few fenestration ideas to transform homes or other structures into a more efficient and visually appealing space:

1.1 Windows Alter Space Perception

Depending upon their size, area and placement, windows have the power to alter the perception of space, and aesthetics. For example, glass-to-glass or corner windows provide terrific views of the landscape. Additionally, strategic selection and placement of windows can help battle climatic fluctuations. Offices and educational institutions with good lighting design have higher productivity. Moreover, it is believed that patients recover faster when they are next to windows in a hospital (Barry, 2011).

1.1 Bay Windows for Scaling Available Space

UPVC bay windows can be used to scale available area. These windows protrude outwards, and with the placement of a divan, they make excellent corner spaces, thus enhancing space utility. They also maximize the influx of natural light and provide amazing views. Bay windows can add elegance to your structure. Moreover, they are known to increase the property value, due to added space and aesthetics (Corgnati et al, 2011).

1.2 Use of Sliding Windows and Doors

If space is limited, sliding windows and doors are ideal. In addition to optimal utilization of space, they also give the perception of a bigger space. They lend a sleek décor and occupy less space, unlike traditional folding doors and windows. Sliding doors are also great for air circulation and panoramic views (Corgnati et al, 2011).

2.4 UPVC for Energy Efficiency

Use of UPVC doors and windows can reduce your energy consumption drastically. Being a poor conductor of heat, UPVC doesn't allow transfer of heat from outside to inside through its surface. When used with double or triple glazing, and air-tight seals, it further insulates against the outside heat. As a result, the internal temperature of the room is maintained and air-conditioner/heater runs less frequently, ensuring lower energy bills. UPVC doors can be used in commercial spaces and residences alike to build environment-friendly structures. A fully recyclable material, UPVC consumes far less energy in its production compared to Aluminium (Corgnati et al, 2011). UPVC also reduces the dependence on wood thereby helping conserve forests. The market is flooded with several glazing options and surfaces for every need. Laminated – glass can be used for insulation against heat and noise. Tinted glass can offer privacy, aesthetics and protection from UV rays, whereas laminated glass can be used for enhanced safety and act as excellent noise insulators, usually necessary for city dwelling (Barry, 2011).

Designers can utilize the abundance of material and fenestration options available in market to make spaces suitable for various weathers. They can prepare the available space to withstand the worst weather through the smart use of new-age framing materials like 'UPVC'. UPVC's inherent weather resistant features prevent windows from getting faded or distorted even when exposed to temperature variations,

moisture or intense UV radiations (Attia et al., 2013). UPVC frames are also reinforced with steel that provides windows with exceptional strength to bear high wind speeds up to 250kmph, making them ideal for high rise apartments.

2.5 Skylight

Skylight is another nifty option for lighting up the space. It provides excellent ventilation and gives a perception of larger space. Many skylights are fitted with UV glass for energy efficiency. They also come with remote-controlled, solar-powered blinds.

2.6 Controlling Daylight in Buildings

2.6.1 Rule of Thumb

The basic shape of a building will impact its ability to use daylighting effectively. Hence, when developing a building shape, consider how best to admit daylight into the building. Building shapes with a narrow floor plate will maximize exterior wall areas to incorporate glazing (Corgnati et al, 2011). These shapes can be elongated, curved, or combinations of multiple shapes. Deep buildings with large floor plates can use atria and courtyards in order to bring daylight into the inner realms of the building. Low-rise and one-story structures have more opportunities for daylighting by using the roof as a daylighting source, thus allowing more shape options (Attia et al., 2013).

According to Attia et al. (2013)ome rules of thumb for creating a building form to maximize daylighting include:

Develop the building shape and floor plates by locating occupied spaces using the 4.5 / 10m rule for typical storey heights: Create a 4.5m perimeter zone depth for task daylighting and an adjacent 4.5m zone for ambient daylighting.

Make the north and south sides of the building longer and more exposed for controlled daylighting by elongating the form in the east-west direction.

Use high ceilings and windows to allow for greater penetration of daylight into the interior. Sloping the ceiling from the high window side down to the interior may help with penetration and distribution as well.

2.6.2 Side Daylighting

The building shape and size will determine whether side daylighting can be achieved on just one side or on multiple sides. Daylighting spaces from multiple sides provide more even lighting while producing less glare. This can be achieved by providing glazing on adjacent or opposite walls or by providing a combination of side daylighting and top daylighting strategies (Corgnati et al, 2011). Spaces daylit from only one side will need to be assessed to avoid a steep light gradient between the daylit side of a room or space and the unlit side. Spaces improperly daylit from one side may contain excessive differences in

brightness, intense contrasts, and uncomfortable glare conditions (Attia et al., 2013).

Some basic rules of thumb for successful side daylighting include:

Acceptable interior task-daylight levels can be achieved at a depth of 1.5 to 2 times the height of a glazed opening in an exterior wall.

A light shelf added to a glazed opening will reflect daylight deeper into a space, and can increase the daylighting depth to 2.5 times the height of the glazed opening.

Size the glazing area as a percentage of the floor area of the space to be daylit. For minimum or ambient lighting, use a glazed area that is equal to 10 to 15 percent of the floor area. For more adequate or task lighting, size the glazing to be 15 to 25 percent of the floor area (or 25 to 40 percent of the exterior wall area).

Make the side walls, back wall, and ceiling a light color to evenly distribute daylight and prevent glare.

2.6.3 Top Daylighting

Allowing daylight to enter a space from above rather than the side of a building is extremely effective. The Romans understood this by incorporating an oculus into roof domes, such as the Pantheon, which adequately illuminated the entire space below. Modern warehouses and big box retail stores use small skylights spread across the roof to effectively illuminate large spaces. All of this works because top daylighting gives access to the entire skydome with brighter and more direct daylighting across the day (Attia et al., 2013). It also allows better distribution of light inside the space just as an electric light is more effective on the ceiling compared to being on the wall. Top daylighting creates a more consistent distribution of daylight, sometimes allows for easier glare control, and for penetrating deeper into the interior of a building (Corgnati et al, 2011).

The general rule of thumb for top daylighting is to make the daylighting glazing area a minimum of 10 percent to 20 percent of the floor area to be daylit. Too little area can create excessive contrast and glare while too much area can overwhelm the space with light. Either way, filtering and distributing the light is beneficial, particularly in critical task areas to avoid direct rays of sunlight from interfering with day-to-day activities (Corgnati et al, 2011).

2.6.4 Daylighting Balance

Whether side daylighting, top daylighting, or a combination is used in a particular building project, the design challenge of balance and control is critical to a successful outcome. Daylighting has direct impacts on things beyond the provision of natural light and views. If the light is too intense or creates too much of a contrast within a space, then it will be regarded as uncomfortable glare that is not welcome by the occupants (Corgnati et al, 2011). The constant exposure of materials and finishes to sunlight can also cause colors to fade and materials to break down. But perhaps the biggest balance issue is the fact that the

solar light entering the space also brings solar heat with it, all year long. That solar heat may be welcome in cool weather, contributing to greater occupant comfort while using less purchased energy for a mechanical heating system. However, during warm weather or in buildings that tend to require more cooling than heating, increased daylighting can bring an unintended penalty of too much solar heating, thus making people less comfortable, causing more air conditioning to run, and consume more energy—all the opposite of our original design intentions (Attia et al., 2013).

1.0 Methodology

This study employed a survey technique in eliciting information on the subject matter. A total of one hundred and fifty professionals were interviewed and questionnaires administered on them and retrieved by the researcher. A 4- point Likert scale was adopted with a maximum score of 4.0 and a criterion mean score of 2.50. The findings of these focus group interviews, questionnaires and personal observations were correlated with existing mathematical relationships of the major factors that affect fenestration and recommendations were made.

1.0 Results and Discussion

Table 1: Major Factors that Affect Fenestration in Building Envelopes

S/N	Factor	Mean Score	Rank
1	Solar exposure	3.25	2
2	Climatic zone	3.10	6
3	Projections and shades	2.96	8
4	Solar heat gain	3.15	4
5	Total area of glazing elements	3.20	3
6	Orientation of glazing elements	3.12	5
7	Thermal conductance / u-values components of the building envelope	3.54	1
8	Total floor area of buildings	3.0	7

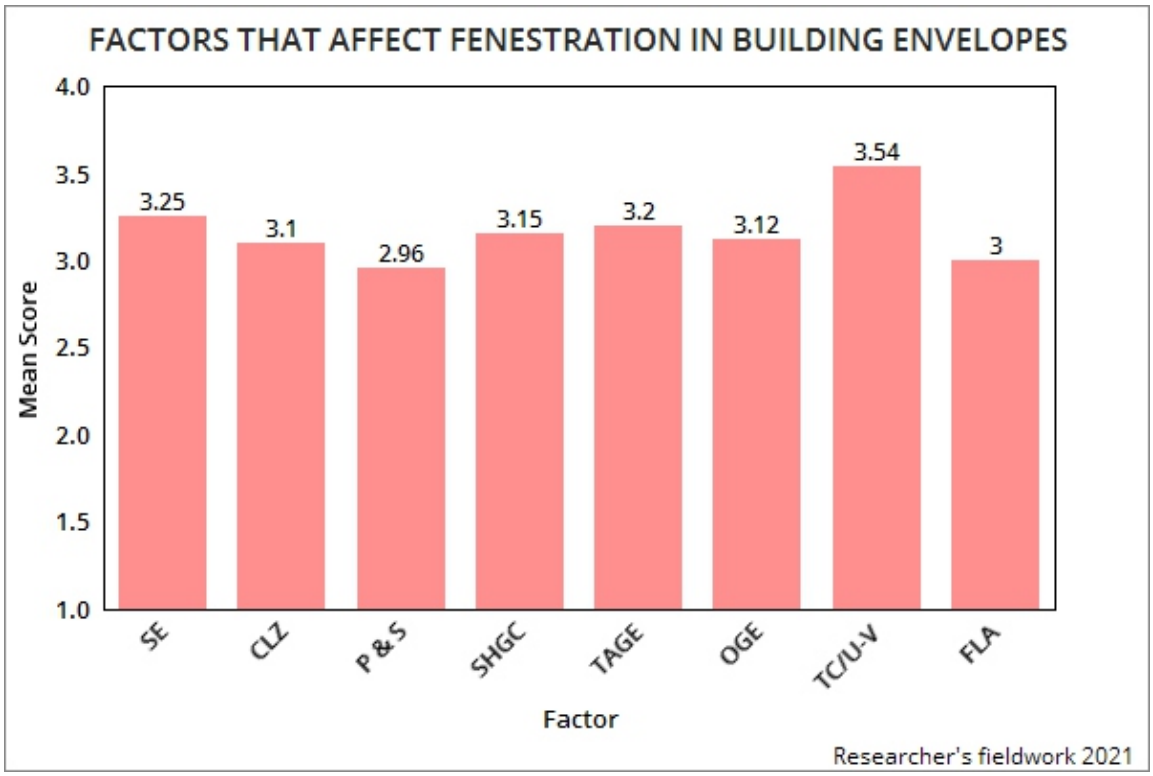

Fig. 1: Major factors that affect fenestration in building envelopes

From Table 1, the major factors that affect fenestration in building envelopes are: solar exposure; climatic zone; projections and shades; solar heat gain; total area of glazing elements; orientation of glazed elements; thermal conductance/ u-values of components of the envelope; total floor area.

4.2 Ranking of Factors that affect Fenestration in Building Envelopes

From Table 1, it could be seen that the major factors that affect fenestration in building envelopes are, in accordance with their ranks: thermal conductance/ u-values of components of the envelope, TC/U-V (1); solar exposure, SE (2); total area of glazing elements, TAGE (3); solar heat gain, SHGC (4); orientation of glazed elements, OGE (5); climatic zone, CLZ (6); total floor area, FLA (7); projections and shades, P & S (8).

5.0 Conclusion and Recommendations

5.1 Conclusion

The issue of fenestration is as old as the concept of building, itself. Thermal comfort in buildings is paramount in design and construction considerations. At the design stage, effective fenestration is affected by: thermal conductance/ u-values of components of the envelope; solar exposure; total area of glazing elements; solar heat gain; orientation of glazed elements; climatic zone; total floor area; projections and shades.

5.2 Recommendations for Effective Computation of Fenestration Requirements in Buildings

5.2.1 Calculate the net floor area of each storey of the proposed building measured within the enclosing walls.

5.2.2 Calculate the total area of the glazing elements of each storey of the proposed building.

5.2.3 Calculate 15% of the net floor area of each storey of the proposed building.15%: (net floor area of storey) ÷ (100) x (15)

5.2.4 Determine whether the total area of the glazing elements for each storey is greater than 15% of the net floor area of such storey. Where the total area of the glazing elements of a storey does not exceed15% of the net floor area of the storey the minimum energy performance requirements for such storey is deemed satisfied. Where the total area of the glazing elements of a storey is greaterthan15% of the net floor area of the storey the requirements contained in SANS 204 shall be complied with. Where the requirements of SANS 204 are to be complied with proceed to 5.3.5.

5.2.5 Identify the Climatic Zone applicable.(refer Annex A - SANS 204)

5.2.6 Identify the relevant constants for conductance and SHGC applicable to the identified climatic zone.(refer table 5 - SANS 204).

5.2.7 Calculate the conductance and solar heat gain (SHGC) values that the glazing in each storey shall not exceed. Max. Conductance: (net floor area of storey) x (constant, CU) Max. Solar heat gain: (net floor area of storey) x (constant, CSHGC)

5.2.8 Calculate the aggregate conductance value for the glazing in each storey by adding together the conductance of each glazing element. Where the conductance of a single glazing element is calculated as follows:

conductance = (area of glazing element) x (U-value of glazing element)The aggregate conductance value of glazing elements is therefore calculated thus (A1xU1) + (A2xU2) + (A3xU3) + (A4xU4) + (A5xU5) + ...

Note: U-values used from table 6 of SANS 204 provide for worst case assessments. The alternative is to use certified U-values from manufacturers (combined effect of glass & frame).

5.2.9 Calculate the aggregate SHGC value for the glazing in each storey by adding together the SHGC of each glazing element. Where the SHGC of a single glazing element is calculated as follows: SHGC = (area of glazing element) x (SHGC-value of glazing element) x (solar exposure factor for the glazing element).

In order to determine the applicable solar exposure factor for a glazing element in a storey the following additional information is required for the glazing element:- the orientation sector of the glazing element -the horizontal length of the shading element (P) that casts a shadow onto the glazing element per storey measured from the face of the glass(Sec. 4.3.5. Shading – SANS 204)-the vertical height (H) from the base of the glazing element to the underside of the shading element used in measuring (P) (Sec. 4.3.5. Shading – SANS 204).

Calculate the value of P/H per glazing element to determine the applicable solar exposure factor:

P/H = (horizontal projection (P)) ÷ (vertical height (H))

Determine the solar exposure factor (E) based upon the P/H value calculated and orientation of the glazing element for the applicable climatic zone.(Annex C – SANS 204)

Upon determining the solar exposure factor the SHGC of the single glazing element can be calculated as follows: SHGC = (area of glazing element) x (SHGC-value of glazing element) x (solar exposure factor for the glazing element) PH

The aggregate SHGC value of glazing elements is therefore calculated thus :(A1 × S1 × E1) + (A2 × S2 × E2) + (A3 × S3 × E3) + (A4 × S4 × E4) + ...

5.2.10 Determine whether the maximum permitted conductance and maximum SHGC for each storey has not been exceeded by comparing the values calculated in 5.2.8 and 5.2.9 against the maximum permitted values calculated in 5.2.7 for conductance and SHGC. Where aggregate conductance, per storey, is less than or equal to maximum conductance permissible and aggregate SHGC per storey is less than or equal to maximum SHGC permissible), the glazing proposed satisfies the requirements of SANS 204 and SANS 10400-XA. Where aggregate conductance per storey is greater than maximum conductance permissible and / or aggregate SHGC per storey is greater than maximum SHGC permissible, the glazing proposed does not satisfy the requirements of SANS 204 and SANS 10400-XA.

5.2.11 Where the glazing per storey proposed does not satisfy the requirements of SANS 204 reconsider the following aspects, individually or in combination with one another:(a) framing system;(b) glazing material;(c) size of glazed elements;(d) extent of shading to glazed elements;(e) orientation of glazed elements, and recalculate the aggregate conductance and SHGC per storey according to 5.2.8 and 5.2.9. Repeat 5.2.8 and 5.2.9 after each adjustment of aspects in 5.2.11 (a)-(e) above until the requirements of SANS 204 are satisfied with respect to conductance and SHGC.

5. 2.12 Where a centrally controlled artificial ventilation or air conditioning system is incorporated into the building proposal, proceed to 5.2.13.

5.2.13 To ensure the future installation of a centrally controlled artificial ventilation or air conditioning system does not compromise the compliance designed in a building, it is suggested that the fenestration calculations for buildings with centrally controlled artificial ventilation or air conditioning systems is undertaken.

Appendices

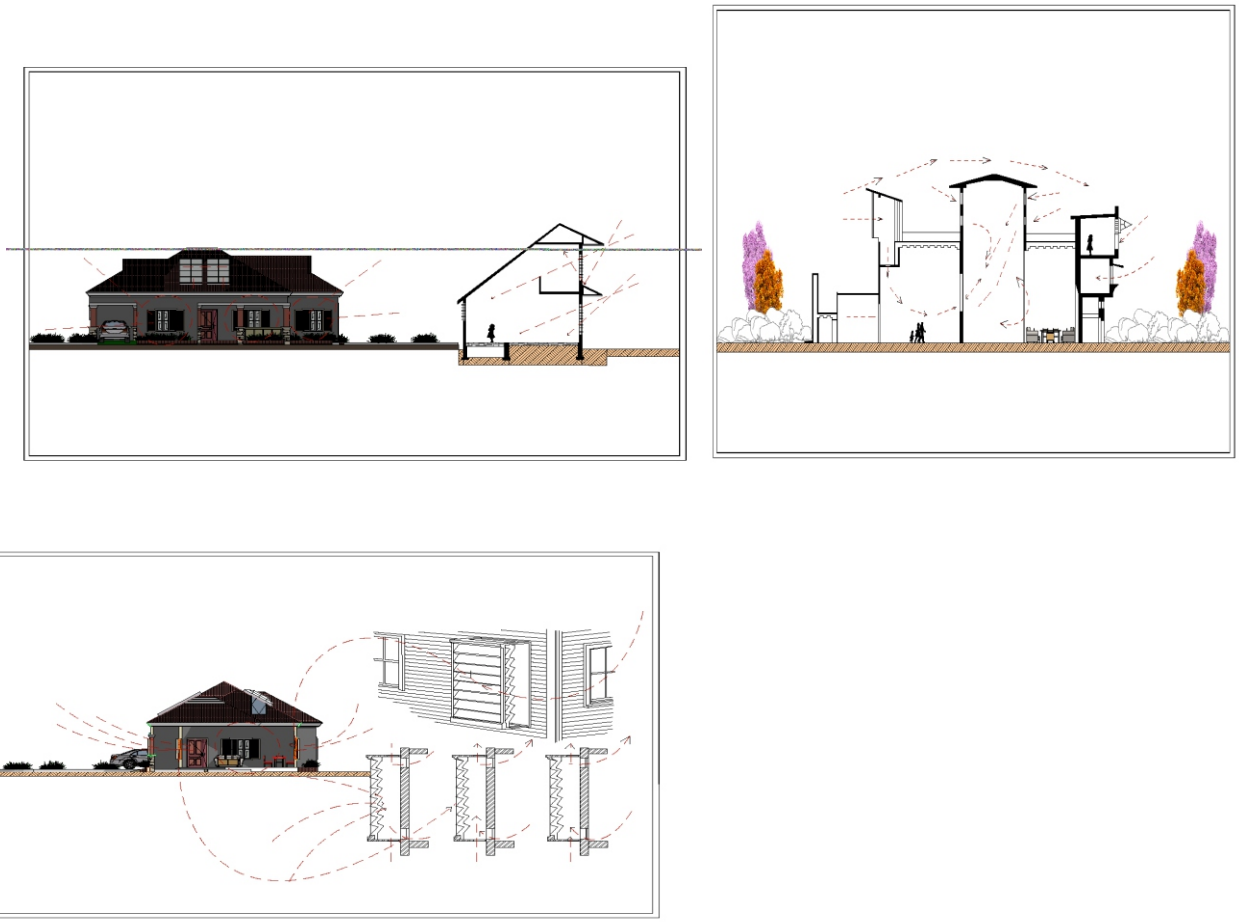

Appendices.1-3: Convectional distribution of natural air in available fenestration in building (Source: Edokpolo, 2020)

References

Afon, A. (2000). "Use of residents' environment quality indicator (EQI) data in a residential housing improvement. In effective housing in the 21st century, Nigeria". M., Fitzgerald (Ed), *The Environment Forum*, 15: 115-122. http://*www.iefworld.org/papers.htm*

Attia, S., Hamdy, M., O'Brien, W and Carlucci, S. (2013). "Assessing gaps and needs for integrating building performance optimization tools in net zero energy buildings design", *Energy and Buildings* 60, 110-124.

Barry, D. (2011). "Ventilation and Occupants' health". *Medcare* 26 (3): 67-73

Corgnati, S. P., Gameiro da Silva, M., Ansaldi, R., Asadi, E., Costa, J.J., Filippi, M., Kaczmarczyk, J., Melikov, A. K., Olesen, B. W., Popiolek, Z., and Wargocki, P. (2011). "*Indoor climate quality assessment – evaluation of indoor thermal and indoor air quality". Rehva Guidebook, 14*. Brussels: Rehva.

Edokpolo, E.L.O (2020). "Assessment of energy efficiency and thermal comfort in residential buildings in some selected residential neighborhoods in the Benin metropolis", Ph.D seminar, Ambrose Alli University, Ekpoma, Edo State.

Fang, L., Wyon, D. P., Clausen, G., and Fanger, P. O. (2004). "Impact of indoor air temperature and humidity in an office on perceived air quality, symptoms and performance". Indoor air. 14 (7), 74–81.

International Panel on climate change, IPCC (2013). *Climate change: The physical science basis I..*

International Panel on climate change, IPCC (2014). *Climate change: The physical science basis II.*

Ruth, J (2016). Window & Door. American Architectural Manufacturers Association.)

SANS 10400-XA & SANS 204 (2011). "Fenestration - natural environmental control Guideline

MODELLING INDOORFORMALDEHYDE EXPOSURE IN A UNIVERSITY HOSTEL BUILDING USING ARTIFICIAL NEURAL NETWORKS

Adekunle, A.A., Nkeshita, F.C.,Owosho, S.S. and Igba, U.T.

Department of Civil Engineering, Federal University of Agriculture, Abeokuta, Nigeria

Abstract

Indoor air quality is gaining more attention from researchers and other stakeholders. Formaldehyde is a major indoor airpollutant that has attracted public attention worldwide due to its negative impact on health and can be found in household and construction products. The data set was comprised of particulate matters (1.0, 2.5, and 10), Total Volatile Organic Compound (TVOC), Relative Humidity, Daily Ambient Temperature, and Formaldehyde. Sample data for Indoor Air Quality were gathered from an active sampler. The data collection was carried out in eighteen days consecutively in one room located on the ground floor of the hostel building located at the Federal University of Agriculture, Abeokuta, Nigeria.The Artificial neural network has proven to be an effective tool in the analysis of non-linear data by establishing a relationship between experimental and predicted data through historical data records. The results of MSE of the tested network indicated the best performance was obtained at 0.00011101 at epoch 1 when a neural network architecture comprising 16 hidden neurons was usedand which was resulted in a coefficient of determination value of **0.98** meaning that the input and output data have a strong positive relationship if one of them decreases, then the other one will follow it and vice versa. The model can be improved upon by adding more indoor environmental parameters and prolonging the duration of data collection to reflect seasonal variations.

Keywords: Artificial Neural Networks, Formaldehyde, Indoor air quality, Air-pollutants

1.0 INTRODUCTION

In recent years, Indoor air quality has been receiving a lot of interest from researchers, policymakers, and other interested stakeholders. This is mainly because of the importance of comfort, health, and wellbeing of the occupants of buildings. In research conducted by the American Lung Association, respondents were aware of the tendency of outdoor air pollution to cause damage to their health but are not aware of the negative health impact that indoor air pollution can also have as well. (Commission, 1996).Thesepollutants found indoors can be higher in concentration than pollutants found outdoors(Vazquez K and Adams L., 2014). According to Crump *et al* in 2009, examples of Indoor air pollutants include Sulphur (IV) Oxide, Volatile Organic Compounds (VOCs), Formaldehyde (HCH0), Carbon Monoxide (CO), Carbon (IV) Oxide (CO_2), Radon, Fibers, Particulate Matter, Ammonia, Nitrogen (IV) Oxide (NO_2), etc.

Certain environmental parameters have been shown by researchers to influence the effects of indoor air pollutants. These include; Relative Humidity, Temperature,and atmospheric pressure. An example is aninvestigation that was carried out by Chen *et al* (2016) on the prevalent levels of certain chemicals and environmental factors which included Carbon dioxide (CO_2), Carbon monoxide (CO), oxygen (O_3),humidity, temperature, formaldehyde, TVOCs, PM_{10} and $PM_{2.5}$, and microbial agent concentrationsin a study area in North Taiwan.Other researches have focused on indoor air quality in schools. An investigation was carried out on the influence of dampness in a house on the occurrence of certain ailments

such as asthma and other respiratory infections among students at the academic institution in Canada (Lanthier-Veilleux M*et al*., 2016).

Formaldehyde is a major pollutant that can be found indoors is attracting a lot of attention from public health officials and other stakeholders due to its negative impact on health. It is a prominent volatile organic compound found in household and construction products. According to (WHO, 2010) Formaldehyde is inflammable and highly reactive at ambienttemperature and can be purchased commercially as an aqueous solution, knownas formalin.

Some of the sources of formaldehyde indoor include furniture, fiberboard, and laminated wood, rubber, paints, adhesive materials, cosmetics, electronics, and paper products (Aydogan and Montoya, 2011; Akbar-Khanzadeh and Park C, 1997 and Kim*et al*., 2010).

Previous reports have shown that formaldehyde causes health defects such as cancer, leukemia, premature birth,and Alzheimer's disease (Aydogan and Montoya, 2011; Vazquez K and Adams L., 2014).

Air quality prediction is necessary for planning, regulation, and control. Thus, artificial neural network (ANN) has been applied for predicting air quality (Barai,*et al*., 2007; Wang et al., 2003)ANN are powerful tools that can handle complex, nonlinear challenges especially in the fieldsof classifying and predicting phenomena (Ordieres*et al.,*2005).The ANN approach is an imitation of the computer brain which is capable of memorizing and recalling several experiences. In technical terms, it is similar to the Human Brains concerning the ability to recognize knowledge by the network through learning and storage of what was learned by an interconnection of neuron strengths as synaptic weights (Haykin, 1994). The ANNs are obtained from computational applications with algorithms and architecture to be extracted from system neuroscience-related (Daponte and Grimaldi, 1998). An example is the multilayer perceptron neural network shown below in figure 1;

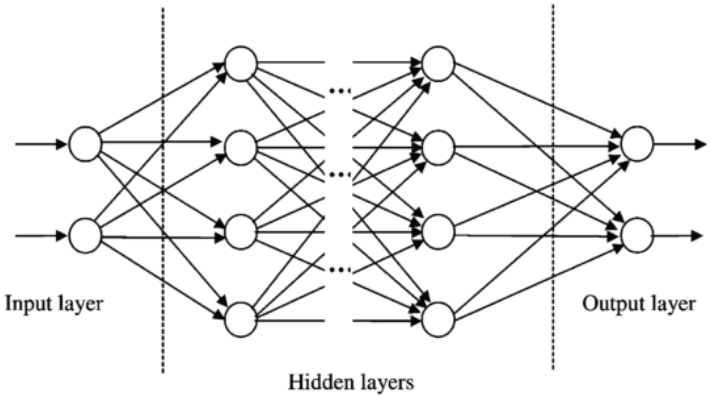

FIGURE 1. A schematic diagram d 2003).isplaying multilayer feed-forward neural network (Kalogirou,

2.0 MATERIALS AND METHODS

2.1 Description of Study Area

The indoor air quality data was collected from a single room at the Iyalode female Hostel located at the Federal University of Agriculture, Abeokuta, South-western Nigeria on 7.232160°N, 3.432887°E.

Figure 2: Map showing Iyalode Female hostel in the Federal University of Agriculture, Abeokuta, South-western Nigeria.

2.2 Data Sets

The set of data that was used in this study are particulate matters (1.0, 2.5, and 10), Total Volatile Organic Compound (TVOC), Relative Humidity, Daily AmbientTemperature, and Formaldehyde.Sample data for Indoor Air Quality were gathered from an active sampler. The collection of data was carried out in eighteen days consecutively in one room located on the ground floor of the hostel building. The measurements for indoor air quality were taken at a standard breathable level of (1.0 - 1.5m) in real-time sampling time in which readings were taken both at 7am and 6pm thus representing estimated periods of peak anthropogenic activity.The sampler was allowed to adjust with the indoor environmental conditions for a minimum duration of fifteen minutes. The average of each daily morning and evening reading was taken for the eighteen days for each environmental parameter. The final data obtained were grouped into input data and target dataas shown in tables 1 and 2. The datasets were normalized between 0 and 1 before being put to use in the neural networks by applying equation 1 (Tardast *et al.*, 2012)

$$Normalized\ values = \frac{(Actual)_{value} - (Minimum)_{actual\ value}}{(Maxiumum)_{actual\ value} - (Minimum)_{actual\ value}}$$

(1)

Table 1. Input Data

DAY	$PM_{1.0}$ (µg/m^3)	$PM_{2.5}$ (µg/m^3)	PM_{10} (µg/m^3)	TVOC	HUMIDITY (%)	TEMP. (°C)
1	6	9	9	1.431	80	25.7
2	6	8	9	0.806	76	26.3
3	3	5	5	3.540	73	36.5
4	3	4	4	1.411	71	26.8
5	6	9	9	0.751	70	26.8
6	6	8	6	0.825	69	27.1
7	3	4	4	3.463	72	26.6
8	3	4	4	3.448	71	27.1
9	1	2	2	0.820	69	27.5
10	1	4	2	0.756	67	26.6
11	3	4	5	0.702	68	26.7
12	14	19	21	0.728	70	26.7
13	19	23	26	0.611	70	27.3
14	52	69	75	0.649	69	27.9
15	14	13	13	0.833	67	27.9
16	3	5	6	0.649	68	26.4
17	3	4	4	0.985	69	25.8
18	3	5	6	0.853	70	26.3

Table 2. Target Data

DAY	HCHO (mg/m^3)

1	0.185
2	0.133
3	0.731
4	0.183
5	0.106
6	0.179
7	0.335
8	0.315
9	0.115
10	0.108
11	0.102
12	0.109
13	0.082
14	0.098
15	0.181
16	0.100
17	0.191
18	0.122

2.3 ANN model for indoor air quality prediction

A three-layer perception model was used comprising the input layer made up of six input variables of the network. These input variables include four pollutants ($PM_{1.0}$, $PM_{2.5}$, $PM_{10,}$ and total volatile organic compound, TVOC) and two comfort variables (Relative humidity and Temperature). One hidden layer was adopted and a set of neurons in the hidden layer were chosen in the model to optimize the ANN performance. The output layer of the prediction modeladopted Formaldehyde concentration as the output variable.The neural network training tool used for the predictive modeling was produced by using MATLAB software. The feed-forward network-back propagation method was applied from the software. In the BP method, theinput data are presented to the network and a corresponding output of the neural network is produced which is comparedwith the desired output and an error is computed. This error isthen channeled back to the neural networkto adjust the weights so that the error decreases with eachiteration and the neural model gets closer and closer to thedesired output. This kindof training involves an optimization process (Sharda, 1994).

The Hyperbolic tangent sigmoid function was used as the transfer function. The given set of data wasdivided into three groups out of which 70% of the datawas adopted in training the networks, 15% designated as the validation set, and the remaining 15% were employed in testing thenetworks. The mean square error (MSE) was adopted as the statistical criteria for measuring the performance of the network.

2.3.1 Training Model

The Levenberg-Marquardt method was used to train the input data due to its capacityto minimize sum-of-squares error functions thereby validating the output data.

2.3.2 Evaluation Model

The network was trained to recognize particular patterns properly. This process was completed using the criteria listed below;

1. Mean Square Error (MSE)measures the average of the squares of the errors or deviations.
2. Regressionis a statistical process for establishing the relationship between the data set.(Lehmann and Casella, 1994)

3.0 RESULTS AND DISCUSSION

The tansig and purelinfunctions were used for the neurons in the hidden layer and output layer respectively. In the training phase, the weights andbiases were adjusted based on gradient-descent back-propagation. The mean square error was adopted as the statistical condition for measuring how the network performed. A total of six input variables comprising $PM_{1.0}$, $PM_{2.5}$, PM_{10}, TVOC, Temperature, and Relative humidity and a single output variable, Formaldehyde was added to create the Neural Network. The models were varied by starting with a minimum of ten neurons as shown in table 3 and subsequently, adjustments were made and Regression analysis performed to investigate the correlation between the actual andpredicted results based on the value of the coefficient of determination, R^2until the best fit results obtained from the neural network were indicated by the correlation coefficient to give the value of 0.98847 as shown in figures 3 and 5. The neural network architecture that produced the best value of R^2 at a minimum value of the mean square error of 0.00011131 is shown below in Figure 4. The result of the neural network architecture when compared to the study conducted by Jouvan*et al*., 2018 in which indoor air quality was predicted using ANN comprising five input variables produced a correlation coefficient of 0.93863. This value was below that obtained for the present study and could be attributed to the network being able to identify patterns connecting input and output data, input data and the training method that was selected had a strong influence on the result of the data prediction.

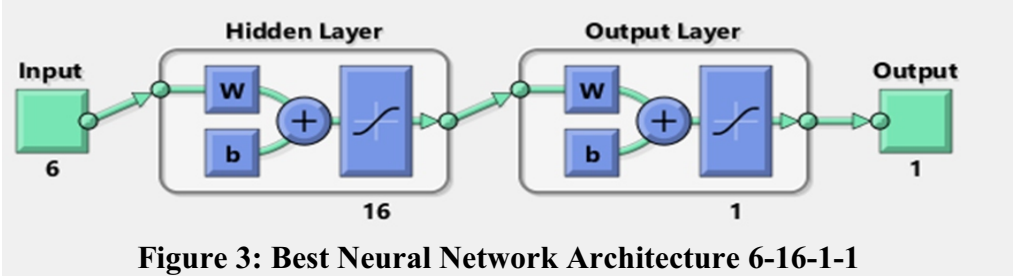

Figure 3: Best Neural Network Architecture 6-16-1-1

Table 3: Structure and training results for the neural network models

Network No	Network structure	Transfer Function	MSE	R^2	Number of Neurons
1	6-10-1-1	Tansig	0.0010694	0.73	10
2	6-13-1-1	Tansig	0.0013922	0.75	13
3	6-15-1-1	Tansig	0.00047723	0.98	15
4	6-17-1-1	Tansig	0.0015679	0.97	17
5	**6-16-1-1**	**Tansig**	**0.00011131**	**0.98**	**16**
6	6-10-1-1	Purelin	0.0042802	0.90	10
7	6-13-1-1	Purelin	0.0003193	0.89	13
8	6-15-1-1	Purelin	0.09185	0.01	15
9	6-17-1-1	Purelin	0.015388	0.74	17
10	6-16-1-1	Purelin	0.00080803	0.50	16

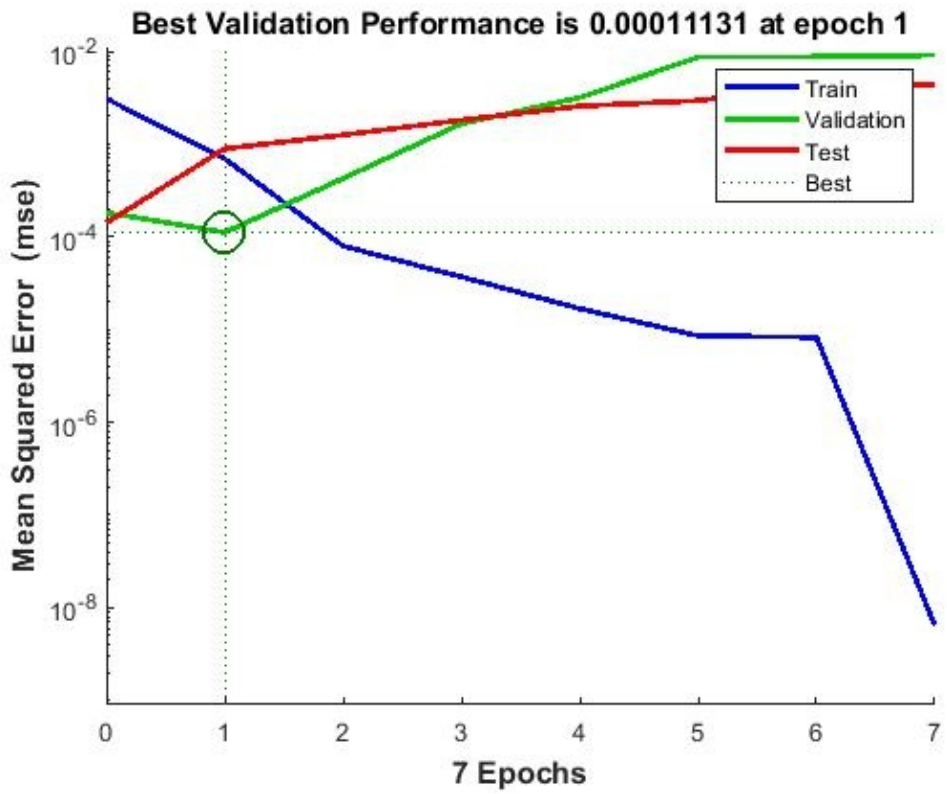

Figure 4: Best validation

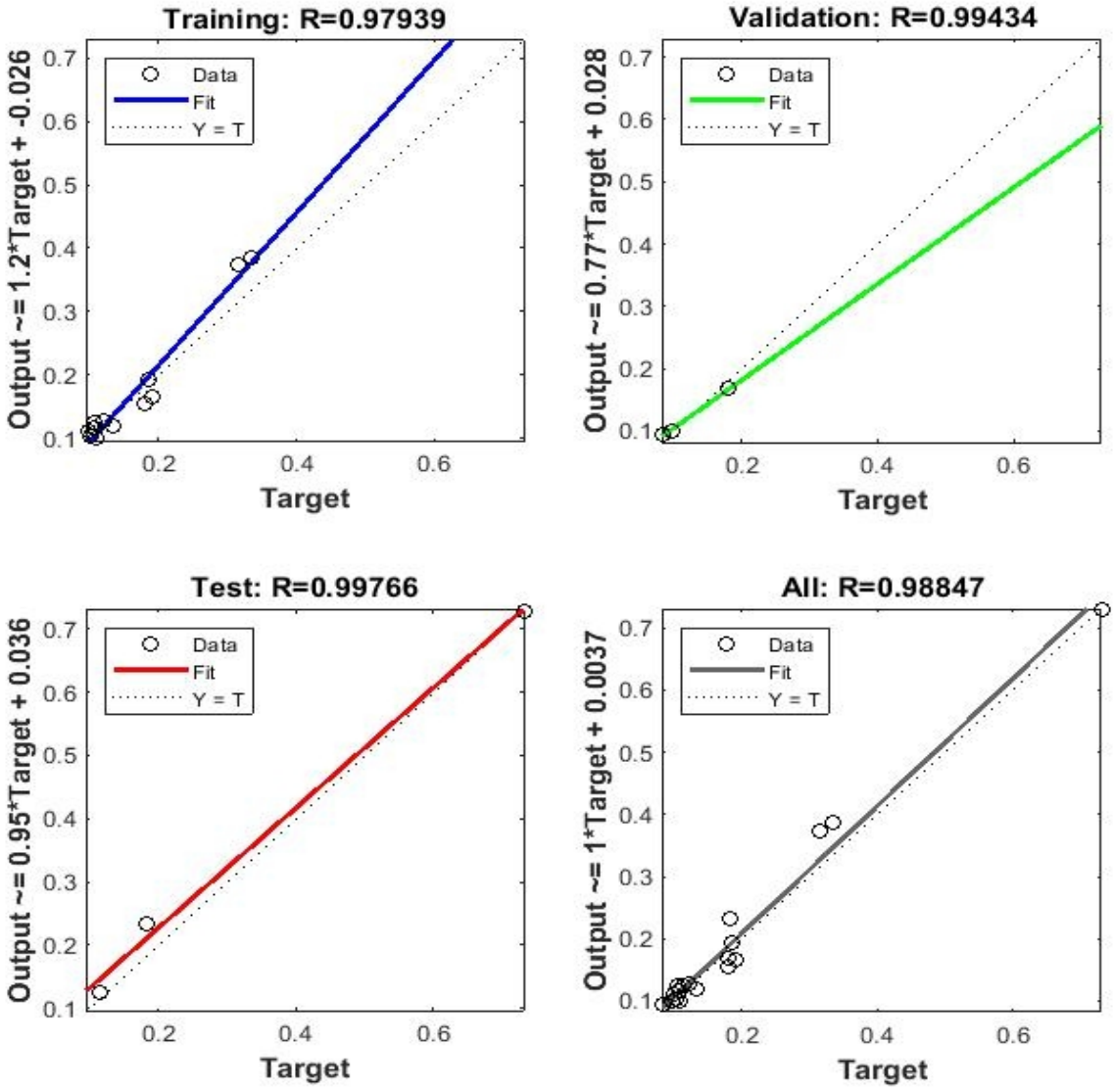

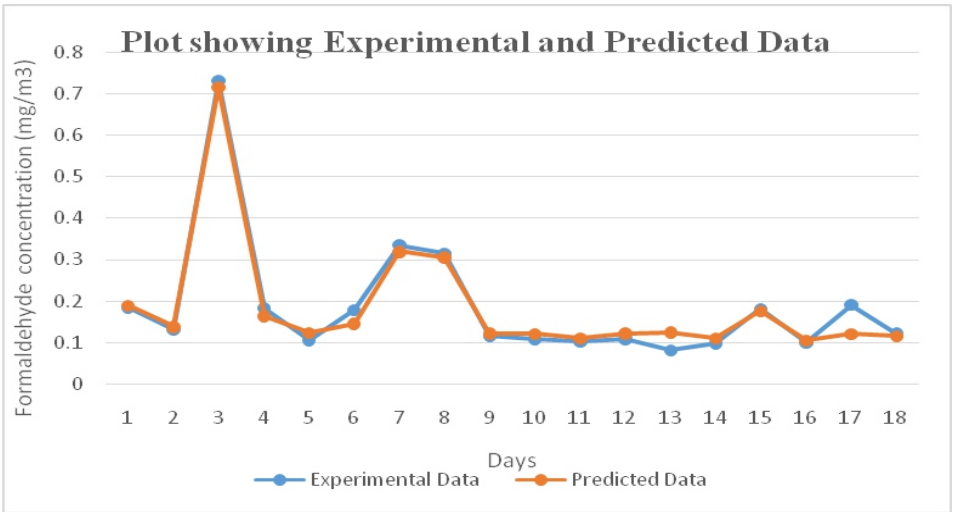

Figure 6: Plot showing Experimental and predicted data of Formaldehyde for the eighteen days

CONCLUSION

The Artificial neural network has proven to be an effective tool in the analysis of non-linear data by establishing a relationship between experimental and predicted data through historical data records. The results of MSE of the tested network as shown in Figure 3 show that the best validation performance was achieved at 0.00011101 at epoch 1 when a neural network architecture comprising 16 hidden neurons was used. Subsequently, the regression test that was carried out to evaluate the capabilityof the tested network towards a particular pattern that has been previously trainedindicated that the tested network can recognize a particular pattern to predict output data. It is characterized by a coefficient of determination value of **0.98**meaning that the input and output data have positive relation, if one of them decreases, then the other one will follow it and vice versa. However, the model can be improved by adding more indoor environmental parameters and prolonging the duration of data collection to reflect seasonal variations.

REFERENCES

Akbar-Khanzadeh F, Park CK. Field precision of formaldehyde sampling and analysis using NIOSH method 3500. Am IndHygAssoc J. 1997;58:657–60.

Aydogan A, Montoya LD. Formaldehyde removal by common indoor plant species and various growing media. Atmos Environ. 2011; 45:2675–82.

Barai, S. V., Dikshit, A. K. And Sharma, S. "Neural Network Models for Air Quality Prediction: A Comparative Study," In: A. Saad, *et al*. Eds., *Soft Computing in Industrial Application*, *Advance in Soft Computing*, Springer- Verlag, Berlin, Vol. 39, 2007, pp. 290-305.

Chen Y., Sung F., Chen M., Mao I. Indoor Air Quality in the Metro System in North Taiwan. Int. J. Environ. Res. Public Health. 2016;13:1200.

Commission, U. C. P. S. (1996). *Indoor Air Pollution: An Introduction for Health Professionals*, Diane Books Publishing Company.

Crump, D., Dengel, A. &Swainson, M. (2009). Indoor Air Quality In Highly Energy Efficient Homes – A Review. *In:* Building Technology Group, B. (Ed.). Institute of Environment and Health, Cranfield University.

Daponte, P andGrimaldi, D., Artificial neural networks in measurements. Journal of Measurement. Vol. 23, no.2, pp. 93–115, 1998. Elsevier.

Haykin S, Neural Networks: A Comprehensive Foundation. New York: Macmillan Publishing, 1994.

Jouvan, C. P.,Safrilah1and Mohammad, I (2018). "*Human-Dedicated Sustainable Product and Process Design: Materials, Resources, and Energy" AIP Conference Proceedings* ***1977****, 020040.*

Kalogirou, S. A. Artificial intelligence for the modeling and control of combustion processes: a review.Journal of Progress in Energy and Combustion Science, vol. 29, no. 6. 2003. Elsevier.

Kim KJ, Jeong MI, Lee DW, Song JS, Kim HD, Yoo EH, et al. Variation in formaldehyde removal efficiency among indoor plant species. Hort Sci. 2010; 45:1489–95.

Lanthier-Veilleux M., Baron G., Généreux M. Respiratory Diseases in University Students Associated with Exposure to Residential Dampness or Mold. Int. J. Environ. Res. Public Health. 2016; 13:1154.

Lehmann, E. L. and Casella, G., 1994. Theory of Point Estimation. Second Edition Springer Texts in Statistics, vol.41, no. 3. 1998.

Ordieres, J. B., E.P. Vergara, R.S. Capuz, and R.E. Salazar. 2005. Neural networkprediction model (PM2.5) for fine particulate matter on the US-Mexico borderin E1 Paso (Texas) and Ciudad Juarez (Chihuahua). Environ. Modell. Softw.20:547–559. doi:10.1016/j.envsoft.2004.03.010

Sharda, R. 1994. Neural networks for the OR/MS analyst: An applicationbibliography. Interfaces 24:116–130. doi:10.1287/inte.24.2.116.

Tardast, A., Rahimnejad, M., Najafpour, G., Pirzade, K., and Mokhtarian, N. (2012). Prediction of bioelectricity production by neural network. Journal *of Biotechnology and Pharmaceutical Research* Vol. 3(3), pp. 62-68.

Vazquez K, Adams L. The Level of Volatile Organic Compounds Exposure in New Buildings: Can Adding Indoor Potted Plants Reduce Exposure? 2014 NCUR. 2014.

Wang, W., Xu, Z. and Lu, J. W. "Three Improved Neural Network Models for Air Quality Forecasting," *Engineering Computations*, Vol. 20, No. 2, 2003, pp. 192-210.

WHO guidelines for indoor air quality for selected pollutants, Regional office report for Europe, 2010.

Xu Z, Wang L, Hou H. Formaldehyde removal by potted plant-soil systems. J Hazard Mater. 2011;192:314–8.

THE EFFECT OF CEMENT STABILIZATION ON THE COMPRESSIVE STRENGTHS OF COMPRESSED EARTH BRICKS PRODUCED IN BENIN CITY, EDO STATE

OBIKORU ONYEKACHUKWU FRANKLIN AND EDOBOR OSEMUDIAMEN RICHARD,
DEPARTMENT OF BUILDING, FACULTY OF ENVIRONMENTAL STUDIES,
AMBROSE ALLI UNIVERSITY, EKPOMA

Abstract

The aim of this study was to determine the effect of cement stabilization on the compressive strengths of compressed earth bricks produced in Benin City, Edo State. The objectives included: the determination of the compressive strengths of cement-stabilized compressed lateritic bricks at different ages; determination of the compressive strengths of cement-stabilized compressed clay bricks at different ages; comparison of the compressive strengths of both cement-stabilized compressed lateritic and cement-stabilized clay bricks. Empirical methods were employed in this study. Samples of reddish-brown laterite and clay were provided for the production of bricks of size 100 x 140 x 290mm and with different percentages of cement- stabilization (0%, 5% and 10%). The results after 28days curing period showed that at 0%, 5% and 10% cement- stabilization, lateritic bricks had compressive strength of 1.12N/mm^2, 1.65N/mm^2 and 2.18N/mm^2 and clay bricks had 1.04N/mm^2, 0.96N/mm^2 and 1.25N/mm^2, respectively. Generally, the brick specimens (irrespective of type) showed improvements when the percentages of the stabilizer increased. The study, therefore, concluded that the use of ordinary Portland cement, as a stabilizer, improved significantly the strength of compressed earth bricks.

Keywords: Compressive strength, earth, clay, laterite, bricks, compressed

1.0 Introduction

Compressive strength is one of the essential mechanical properties to characterize the stress bearing capacity of most construction materials (Billong et al., 2018). Compressed cement-stabilized earth-block construction is currently a popular topic, with growing interest due to its high levels of sustainability and thermal and acoustic performance, the low energy required for production and transport, the decrease in landfill waste, its fire resistance, and the cost of the raw material (CDE, 2000). Compressive strength of brick is important as an indicator of masonry strength and as a result brick strength has become an important requirement in brickwork design. A considerable amount of past research and studies on masonry indicated that stronger bricks contribute to greater brickwork strength (Hendry, 1990). The British standards (BS, 3921, 1985; BS 5628-1, 1992) categorized compressive strength into classes of engineering A and B for construction with aesthetics and strength requirements. All other brick and damp proof- course bricks should have strengths not less than 5 N/mm^2.

Compressed cement-stabilized earth-block construction is a feasible solution for sustainable buildings in many developed and developing countries because cement-stabilized earth blocks offer a number of advantages, such as simple construction methods and maximal utilization of local materials

(Venkararama et al., 2003). Much research has been undertaken to investigate the mechanical properties of compressed cement-stabilized earth blocks (BS 5628-1, 1992).The considerable variation of the composition of earth makes more important the measurement of the compressive strength of compressed earth block and skilled masons to find the optimum composition during the block manufacture (Olivier et al., 1987). Compaction of moist soil, often combined with 4-10% cement stabilization, significantly improves compressive strength and water resistance in comparison with traditional adobe blocks. Dimensional stability and tolerances are also much improved, allowing construction procedures similar to fired clay and concrete block masonry, rather than the wet hand moulded method generally used for adobe. Quality control strength testing of compressed earth blocks has often followed procedures developed for fired clay and concrete block units (Walker, 1996). However, the suitability of these procedures has largely not been checked by scientific study. The compressive strength of compressed earth blocks can be many times lower than similar fired bricks. Previous studies have reported on the compressive strength characteristics of compressed earth blocks (Lunt, 1980). Strength is improved by compactive effort (density) and cement content (generally linear correlation), but reduced by increasing moisture content and clay content (cement stabilized blocks). National and international standards have also developed for compressed earth block test procedures (Walker, 1996; CDE, 2000). However, unlike other masonry units, there is little general consensus on test procedure for compressed earth blocks.

The strength of a soil can be increased 400% to 500% with the use of the correct method for stabilization. Particularly effective strategies of soil stabilization include increasing the soil density as well as adding stabilizing agents, which either react with the soil grains or bind them together (Adam & Agib, 2001). There are several types of stabilizing agents that are commonly used in building CEBs. These include cement, lime, bitumen, gypsum, and pozzolanas. Cementation can make soil water-resistant through the limitation of swelling and the augmentation of compressive strength (Rigassi & Terre, 2015; Reddy & Gupta, 2005) When ordinary Portland cement hydrates when water is added, a cementitious gel is produced that is independent of the soil. This gel is made up of calcium silicate hydrates and calcium aluminate hydrates, which make up the bulk of the gel, and hydrated lime, which is deposited as a separate crystalline solid phase (Millogo & Morel, 2012) This cementation process—which varies with time, temperature, soil type, and cement type—deposits an insoluble binder between the particles of the soil, which embeds them in a matrix of cemetitious gel. At the same time, the lime released during cement hydration forms additional cementitious bonds as it reacts with the clay particle (Mansour et al., 2016).

Research suggests that optimal levels of stabilization occur when the bricks contain between 3% and 18% of cement content by weight. The correct percentage of cement to use depends primarily on the soil type, since the amount of linear shrinkage affects the cement content that is needed for stabilization (Minke, 2006; Holliday et al., 2016). In Benin City, Edo State, compressed earth bricks have been in use, especially for the construction of traditional buildings in line with the Bini culture but these bricks, made majorly from clay have been experiencing a lot of deterioration and poor strength properties. Investigation into the use of alternative soil material has, therefore, become necessary; hence this study.

The aim of this study was to determine the effect of cement stabilization on the compressive strengths of compressed earth bricks made from lateritic soil and clay obtained in Benin City.

The specific objectives were to:

a. determine the compressive strengths of cement-stabilized compressed lateritic bricks at different ages and percentage stabilization;

determine the compressive strengths of cement-stabilized compressed clay bricks at different ages and percentage stabilization;

b. determine the compressive strengths of cement-stabilized compressed clay bricks at different ages and percentage stabilization;

c. Compare the compressive strengths of both cement-stabilized compressed lateritic and cement-stabilized clay bricks at different ages and percentage stabilization.

2.0 Research Methodology

2.1 Research Design

This study adopted an empirical research design. This was necessary so as to achieve more accurate results using a controlled laboratory environment.

2.2 Materials and Methods

2.2.1 Earth Characterization and Preparation

Preliminary tests on the soils that were used were evaluated first for the purpose of classifying and identifying the types of soils. The tests performed were as follows: Soil Particle Size Test, Jar test (sedimentation) Moisture Content Test, Specific Gravity Tests, the Atterberg Limits Tests, linear shrinkage and Compaction Factor Test in accordance with BS1377: Part 2:1990. In order to obtain initial uniform moisture content, the soils were stored under a shed at a room temperature of 22°C for some weeks before being broken down. In order that the stored soil could dry out more evenly, the samples were thinly spread out and regularly turned over several times. Attempts were also made to provide some information about the equipment that was most fundamental for the success of this work. The laterite samples were air–dried for seven days in a cool, dry place. Air drying was necessary to enhance grinding and sieving of the laterite. After drying, grinding was carried out using a punner and hammer to break the lumps present in the soil. Sieving was then done to remove over size materials from the laterite samples using a wire mesh screen with aperture of about 6mm in diameter as recommended by Holliday et al. (2016). Fine materials passing through the sieve were collected for use while those retained were discarded.

2.2.2 Preparation of Brick Samples

The bricks were produced using a locally fabricated wooden mould of size 100x140x290mm. The production process comprises batching, mixing, casting and compaction of the bricks. The materials used for the production of bricks were measured by weight in accordance with the predetermined percentages of stabilization (0%, 5% and 10%) and the optimum moisture contents determined from the field. According to NBRRI, one bag of cement (50kg) with 9 wheel barrows of laterite at a maximum of 5% cement stabilization will give 120 bricks. Therefore, the batching information was gotten from this based on the number of bricks needed.

2.2.2 Preparation of Brick Samples

The bricks were produced using a locally fabricated wooden mould of size 100x140x290mm. The production process comprises batching, mixing, casting and compaction of the bricks. The materials used for the production of bricks were measured by weight in accordance with the predetermined percentages of stabilization (0%, 5% and 10%) and the optimum moisture contents determined from the field. According to NBRRI, one bag of cement (50kg) with 9 wheel barrows of laterite at a maximum of 5% cement stabilization will give 120 bricks. Therefore, the batching information was gotten from this based on the number of bricks needed.

Table 1: Batching Information for Laterite Samples Used

% of stabilization	Laterite (kg)	Cement (kg)	Water (kg)	Water/cement ratio
0	87.6	-	10	8
5	87.6	5	12.2	2.44
10	87.6	10	14.1	1.41

Table 2: Batching Information for Clay Samples Used

% of stabilization	Laterite (kg)	Cement (kg)	Water (kg)	Water/cement ratio
0	78.4	-	10.5	8
5	78.4	5	13.4	2.68
10	78.4	10	15	1.5

The mixing was performed on an impermeable surface made free (by sweeping and brushing or scraping) from all harmful materials that could alter the properties of the mix. The measured laterite sample was spread using a shovel to a reasonably large surface area. Cement was then spread evenly on the laterite and mixed thoroughly with the shovel. The dry mixture was spread again to receive water, which was added gradually while mixing until the optimum moisture content of the mixture was attained. According to Bolyn (2018), a standard 9 liter capacity bucket holds about 15kg of dried soil. The optimum moisture content (OMC) of the mixture was determined by progressively wetting the soil, collecting handfuls of the soil, compressing it firmly in the fist, then allowing it to drop on a hard and flat surface from a height of approximately 1.0 m. When the soil breaks into four or five parts, the water content is considered correct (National Building Code, 2006).

After the wooden mould was rid of all impurities, it was coupled together and oiled to enhance the demoulding of the blocks. The wet mixture was filled into the mould in 2 layers, with each layer being compacted on a level and rigid platform. The excess mixture was scraped off, and the mould was levelled using a straight edge. The mould and its contents were left for two hours before the removal of the mould. The bricks were first allowed to air dry for 24 hours under a shade constructed from a polythene sheet. Thereafter, water was sprinkled on the bricks in the morning and evening, and the bricks were covered with a

polythene sheet for one week to continue the curing process and prevent rapid drying of the blocks, which could lead to shrinkage cracking. The blocks were later stacked in rows and columns until they were ready for strength and durability tests.

Plate 1: brick samples after productiion

2.2.3 Testing of Bricks

Compressive strength tests were performed to determine the load-bearing capacities of the bricks. The dry compressive strengths were determined. For the dry compressive strength tests, the bricks aged 7, 14, 21 and 28 days were transported from the curing or stacking area to the laboratory two hours prior to the test to normalize the temperature and to ensure that the brick was relatively dry. The weight of each brick was measured before the brick was placed onto the compression testing machine such that the top and bottom, as moulded, lied horizontally on a flat metal plate. The brick was then crushed, and the corresponding failure load was recorded. The crushing force was divided by the sectional area of the brick to arrive at the compressive strength. This formula was used in the determination of the compressive strength:

$$Cs = \frac{Cf}{A}$$

where: Cs = compressive strength

Cf = crushing force

A = sectional area

Plate 2: Compressive strength test

3.0 Data Presentation and Analysis

3.1 Data Presentation

Table 3: Compressive strengths of brick samples at 0% stabilization

	Days	Laterite	Clay
Dry mass	7	3.45	
	14	7.55	6.75
	21	6.75	7.30
	28	6.60	6.60
Dry density	7	1797.50	
	14	1859.00	1662.00
	21	1662.00	1797.50
	28	1625.00	1625.00
Dry crushing force	7	16.00	
	14	35.10	10.70
	21	36.25	25.65
	28	45.35	42.35
Dry compressive strength	7	0.39	
	14	0.86	0.26
	21	0.89	0.63
	28	1.12	1.04

Source: field work (2018)

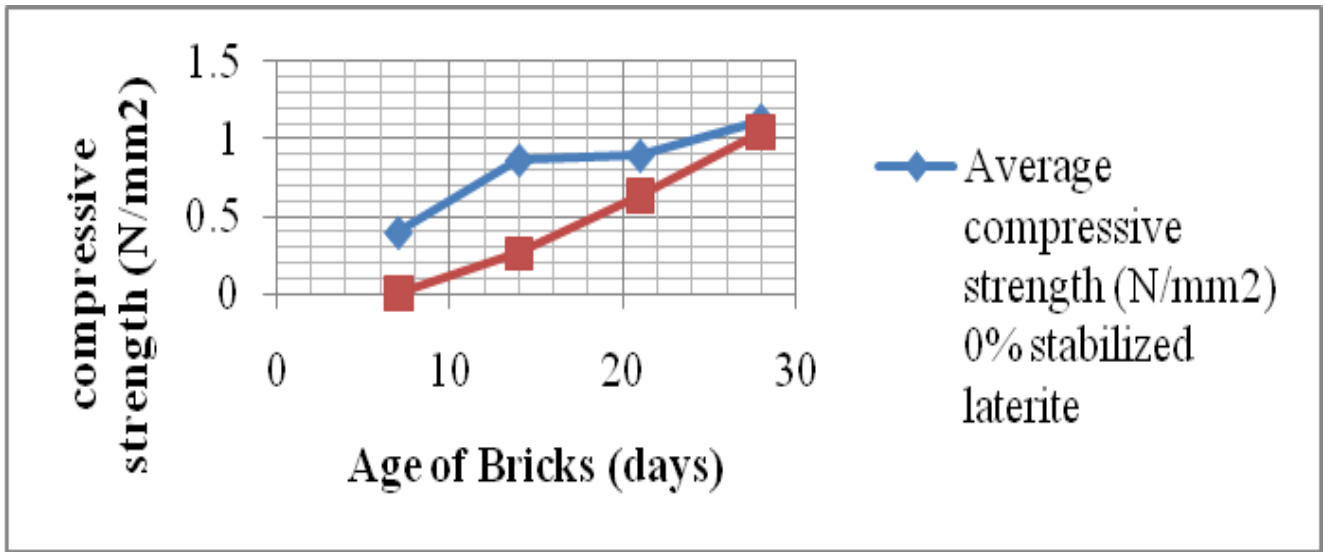

Fig.1: Graph showing comparison of compressive strength development for 0% cement-stabilization for both clay & laterite samples

Table 4: Compressive strengths of brick samples at 5% cement- stabilization

	Days	Laterite	Clay
Dry mass	7	6.80	7.95
	14	6.85	6.85
	21	7.00	6.70
	28	5.65	6.55
Dry density	7	1674.50	1958.00
	14	1686.50	1687.00
	21	1723.50	1649.50
	28	1391.00	1612.50
Dry crushing force	7	32.00	13.90
	14	51.00	21.30
	21	67.00	32.25
	28	67.20	34.40
Dry compressive strength	7	0.78	0.34
	14	1.26	0.53
	21	1.65	0.80
	28	1.65	0.96

Source: field work (2018)

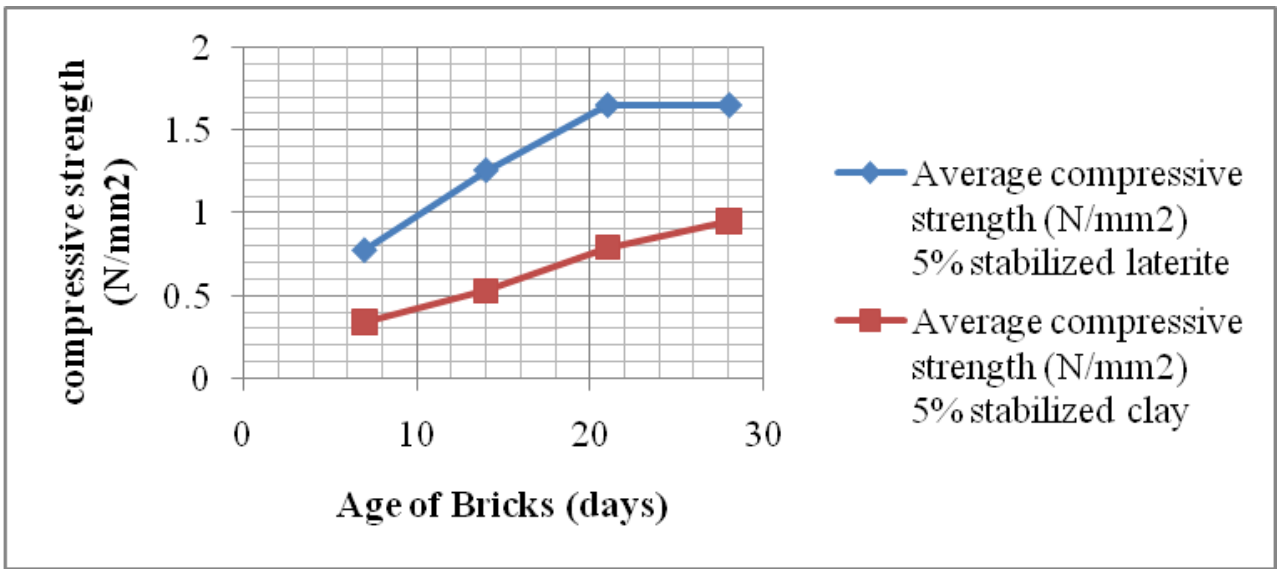

Fig.2: Graph showing comparison of compressive strength development for 5% cement-stabilization for both clay & laterite samples

Table 5: Compressive strengths of brick samples at 10% cement- stabilization

	Days	Laterite	Clay
Dry mass	7	7.65	6.90
	14	6.85	6.50
	21	6.80	6.50
	28	6.25	5.80
Dry density	7	1883.50	1699.00

	21	1674.50	16.50
	28	1539.00	1430.00
Dry crushing force	7	31.25	25.15
	14	36.40	33.90
	21	71.25	42.35
	28	88.75	51.10
Dry compressive strength	7	0.77	0.62
	14	0.90	0.84
	21	1.76	1.256
	28	2.18	1.04

Source: field work (2018

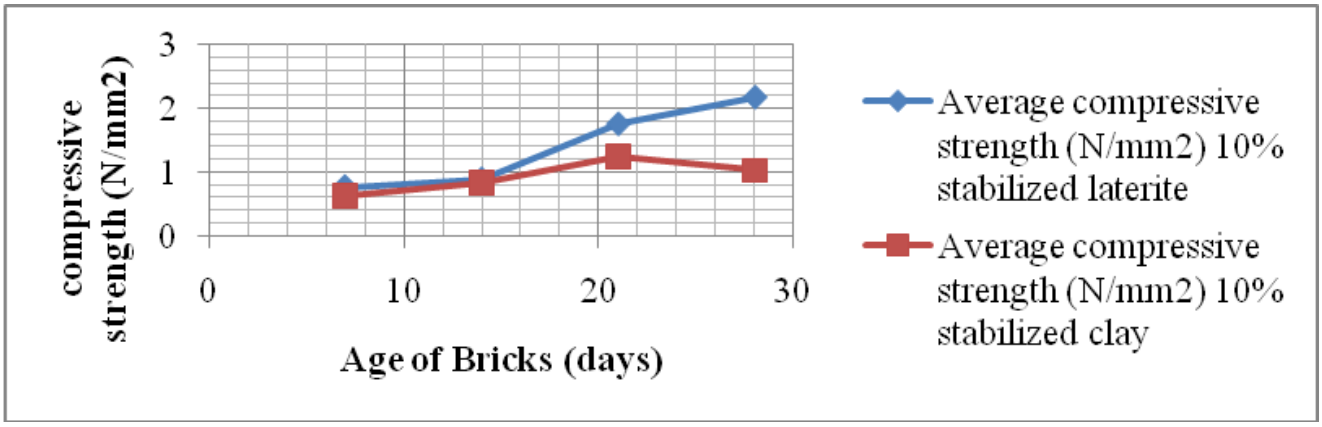

Fig. 3: Graph showing comparison of compressive strength development for 10% cement-stabilization for both

clay & laterite samples

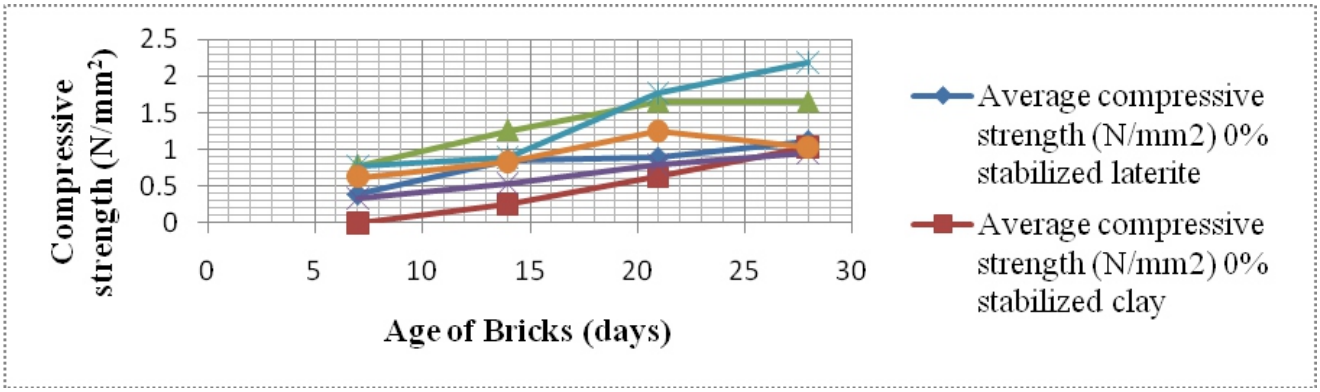

Fig.4: Graph showing comparison of compressive strength development for all percentages of stabilization for both clay & laterite samples

3.2 Discussion of Results

The results of the compressive strengths are presented in tables and figures above for laterite and clay CSEB. It was observed from the tables and figures that the compressive strength of cement -stabilized compressed earth bricks increased as the percentage of cement- stabilization increased. The compressive strength of unstabilized bricks with 0% stabilization (the control) varied from 0.39 N/mm^2 to 1.10 N/mm^2 as the curing age increased from 7 to 28 days. For cement- stabilized laterite bricks, it varied from 0.76 N/mm^2 to 1.65 N/mm^2 and from 0.92 N/mm^2 to 2.18 N/mm^2

for 5% and 10% stabilization, respectively, during the same period. The minimum 7 days dry compressive strength for 5% cement stabilized bricks of not less than 1.60N/mm^2 as recommended by National Building Code (2006) could not be satisfied. The 28 days dry compressive strength of manually produced bricks with 5% cement stabilization, of not less than 2.0N/mm^2 as recommended by NBRRI (2006) was also not satisfied.

Beyond 5% cement stabilization however, all the bricks satisfied the minimum 28 days dry compressive strength. Since lateritic bricks with 5% cement stabilization did not satisfy the minimum requirements as specified by the operating codes, 10% stabilization was recommended for use. The 7 days strengths could not be determined as the samples were very weak to be crushed. The compressive strength varied from 0 N/mm^2 to 1.04 N/mm^2, for 0% stabilization. It also varied from 0.34 N/mm^2 to 1.06 N/mm^2 and from 0.61 N/mm^2 to 1.47N/mm^2 for 5% and 10% stabilization, respectively, as the curing age increased from 7 to 28 days. None of the bricks met the minimum requirements at 7 and 28 days as specified by the available codes. This was due to the fact that the clay had very high mud content; and therefore, could not bear the compressive stress imposed.

4.0 Conclusion and Recommendations

4.1 Conclusion

In the light of the results of experimental tests reported in this study it could be concluded that laterite soil is more suitable than clay for CEB production. The dry compressive strength values obtained for all the stabilized earth bricks were within specified limits and suitable for single storey dwelling. Apart from bricks, without stabilization, all other bricks had dry compressive strength in excess of the minimum strength requirements for masonry in most codes, confirming their suitability for two or three storey buildings. It is appropriate to conclude that the use of Ordinary Portland cement significantly improved the strength of compressed earth bricks.

4.2 Recommendations

From the outcome of this current study the following recommendations were made:

a. Block press be used in molding the bricks rather than using the proctor hammer in an improvised mould;
b. Ordinary Portland cement should be incorporated at a minimal 10% content as a stabilizing agent to improve, significantly, the strength of compressed earth bricks
c. In selecting suitable soil for compressed bricks production, laterite, instead of clay, from different locations should be collected and investigated for their suitability rather than selection based on availability and social acceptance.

References

Adam, E. A., & Agib, A. R. (2001). *Compressed Stabilized Earth Block Manufacture in Sudan.* Paris, France: Graphoprint for the United Nations Educational, Scientific and Cultural Organization,

UNESCO.

Billong, N., Melo, U. C., Louvet, F., & Njopwouo, D. (2008). Properties of compressed lateritic soil stabilized with a burnt clay-lime binder: Effect of mixture components. *Construction and Building Materials* , 2457-2460.

British Standard 5628-1: 1992. Code of practice for use of masonry –Part 1: Structural use of unreinforced masonry. BSI.

British Standards Institution (1985). British Standard Specification for clay Brick. London, BS, p. 3921.

BS 1377. (1990). *Methods of Testing of Soils for Civil Engineering Purposes.* London United Kingdom: British Standard Institute.

Centre for the Development of Enterprise, CDE. (2000). Compressed earth blocks testing procedures, CDE, Brussels, Belgium.

Hendry, A.W. (1990). Structural Design of Masonry Buildings. ISBN 0333497481.

Holliday,L., Ramseyer,C., Reyes,M., and Butko, D. (2016). "Building with compressed earth block within the building code," *Journal of Architectural Engineering*, vol. 22, no. 3, Article ID 04016007.

Lunt, M.G. (1980). Stabilised soil blocks for building, Overseas Building Notes, Building Research Establishment, Garston.

Mansour, M. B., Jelidi, A., Cherif, A.S., and Jabrallah, S.B.(2016). "Optimizing thermal and mechanical performance of compressed earth blocks (CEB)," *Construction and Building Materials*, vol. 104, pp. 44–51.

Millogo, Y., and Morel, J.C. (2012). "Microstructural characterization and mechanical properties of cement stabilised adobes," *Materials and Structures*, vol. 45, no. 9, pp. 1311–1318.

Norton, J. (1997). *Building With Earth: A handbook.* London: Intermediate Technology Publications.

Olivier, M., Mesbah, A., El Gharbi, Z. and Morel, J.C. (1997). Test method for strength test on blocks of compressed earth, Materials & Structures, 30, November, 515-517 In French.

Reddy, B.V.V., and Gupta, A. (2005). "Characteristics of soil-cement blocks using highly sandy soils," *Materials and Structures*, vol. 38, no. 6, pp. 651–658.

Rigassi, V., & Terre, P. (1985). *Compressed earth bricks: Manual of production* (Vol. I). Germany: Deutsches Zentrum fur Entwicklungs technologies-GATE.

Tripura, D.D., and Singh, K.D. (2015). "Characteristic properties of cement-stabilized rammed earth blocks," *Journal of Materials in Civil Engineering*, vol. 27, no. 7, Article ID 040414214.

Venkatarama, R. B.V., Sudhakar, M. R., and Arun, K.M.K. (2003). Characteristics of stabilised mud blocks using ash-modified soils, The Indian Concrete Journal, February, 903-911.

Walker, P. (1996). Specifications for stabilized pressed earth blocks. *Masonry International , 10* (1), 1-6.

BASIC PLASTIC DAMAGE CONSTITUTIVE MODELS FOR ASSESSING CONCRETE FAILURE

O. H. Aliyu[1] and A. A. Salihu

(Department of Building, Faculty of Environmental Sciences: The Federal University Birnin Kebbi,)
(P.M.B. 1157, Birnin Kebbi, Nigeria)
Corresponding author's email address: ohunene.hafsa@fubk.edu.ng

Abstract

This work highlights on the theories behind the basic plastic damage equations used in assessing the failure of reinforced concrete material under applied load. Here, the plastic flow rule, yield function, damage variable, hardening variables as well as the loading and unloading function for both plasticity and damage have been discussed. A numerical example assessing the damage of a 3D reinforced concrete beam in Abaqus using the concrete damage plasticity model was carried out. The model gave good predictions of the crack pattern in the reinforced concrete beam as the tension in the beam increased under action of the applied load showing the strength of the method in assessing concrete damage.

Keywords: Damage variable, plasticity, flow rule, hardening parameters, dilatancy

1.0 Introduction

The failure behaviour of concrete under loading can be captured using plastic theory and damage mechanics models at the micro-structural level with the changes observed at this level incorporated into a continuum model using predetermined set of scalar or tensor valued internal variables (De Brost et al. 2012). These failure modes of concrete which typically entails cracking of concrete in tension and compression are generally characterised by irreversible deformations as well as inelastic volumetric expansion in concrete in addition to the decay in concrete elastic stiffness (i.e. a decrease in stress under rising strains which entails softening) as well as increase in stress with rising deformation which entails hardening Grassl and Jirasek (2006); Grassl et al. (2011); Xotta et al, (2014); ultimately, resulting in the loss of material stability as well as a loss of elipticity of the governing equations (De Brost et al. 2012). In addressing these complex behaviours of concrete material under loading, adopting the plastic flow theory ensures that the irreversible deformations as well as the inelastic volumetric expansions are properly captured (Lubliner, 2008; Rouquand et al. 2007; Xotta et al, 2014). Similarly, damage mechanic models are equally used to capture the loss or decay of concrete stiffness (Lubliner et al. 1989; Rouquand et al. 2007; De Brost et al. 2012). Coupling both plasticity and damage models allows for plasticity (together with hardening) to be augmented with any of the isotropic or anisotropic damage models (Xotta et al, 2014). But because of the complex nature of the anisotropic damage model its combination with plasticity theory is not easy, hence, a combination of the isotropic damage models with plasticity theory is considered the more favoured approach for concrete since for the isotropic models for the stress state can be evaluated directly, exclusive of any iterative calculations (Salari et al. 2004; Grassl and Jirasek 2006; Grassl 2011). The objective of this study is to highlight on the theories behind the basic plastic damage equations used in assessing the failure of reinforced concrete material under applied load. These theories have been implemented in most of the finite element packages. In Abaqus, it boils down to simple options which need to be turned on to carry out damage assessment of concrete structures under load. For this study, we have carried out a numerical example using Abaqus to show the strength of these coupled damage plasticity theories in assessing failure in a simple reinforced concrete beam under uniformly distributed pressure load.

Nomenclature

$\dot{\lambda}$ – is the plastic rate multiplier
$\dot{\mu}$ – is the damage multiplier
m – is the direction of plastic flow
n –gradient of the yield surface
γ – is a scalar quantity.
Ψ – is the plastic flow potential
K –is the thermodynamic conjugate force for plasticity
Y –is the thermodynamic conjugate force for damage
$r(D)$ – is the energy resistance function
g^p – is the potential function for plasticity
g^p – is the potential function for damage
$\bar{e}^p$ – is the effective deviatoric plastic strain
J_2 –is the second invariant of the devatoric stress tensor
D or ω – is the scalar valued damage parameter
$\dot{\lambda}$ – is the plastic rate multiplier that determines the magnitude of the plastic flow rate
$\dot{\epsilon}^p$ –plastic flow rate
$\bar{\sigma}$ – is the effective stress
$\bar{\sigma}_t$ – positive part of the effective stress tensor
$\bar{\sigma}_t$ – negative part of the effective stress tensor
$\bar{\sigma}_v$ –volumetric effective stress
ω_t and ω_c –scalar damage parameters
σ – is the yield strength
$\bar{\varepsilon}$ – is the effective plastic strain
D^s – is the fourth order secant stiffness tensor
D^e –is the elastic stiffness
ϵ^p – is the plastic strain in concrete
ϵ^e –is the elastic strain tensor
$\hat{\sigma}$ – is the effective stress
$\dot{\bar{\sigma}}$ – is the effective stress rate
k – is the internal variable whose value depends on the equivalent stain
ω – is the damage variable describing the amount of isotropic damage
ϵ – is the total strain in concrete
E – is the total stiffness
f_d – is the damage loading function
k_d – is the damage hardening variable
K^0 – Initial bulk density
$r(D)$ – Energy resistance function
r_0 – Modulus of resilience
α – Material friction
I_1 – First invariant of the deviatoric stress
J_2 – Second invariant of the deviatoric stress
α_r – depends on the rate of concrete
α_c – used to distinguish between tensile and compressive stress states
x_s – ductility measure

2.0 Literature Review

2.1 Basic Principles of Plasticity and Damage models

Before discussing coupled plasticity and damage models, the basic principles of both plasticity and damage are discussed here.

2.2 Flow theory of plasticity

2.1.1 Constitutive equations

Unlike in elasticity where we have a one-to-one relationship between stress and strain as given in equation (1)

$$\boldsymbol{\sigma} = \boldsymbol{D^e}: \boldsymbol{\epsilon^e} \ldots\ldots\ldots\ldots\ldots\ldots\ldots\ldots (1)$$

For plastic deformations, no such relationship exists; rather we work with the rate of form where the stress rate is related to the strain rate.

$$\dot{\boldsymbol{\sigma}} = \boldsymbol{D}: \dot{\boldsymbol{\epsilon}} \ldots\ldots\ldots\ldots\ldots\ldots\ldots\ldots (2)$$

Here, the total strain ($\boldsymbol{\epsilon}$) is obtained by a straightforward differentiation of equation 3

$$\boldsymbol{u} = \boldsymbol{u}^e + \boldsymbol{u}^p \ldots\ldots\ldots\ldots\ldots\ldots (3)$$

$$\boldsymbol{\epsilon} = \boldsymbol{\epsilon}^e + \boldsymbol{\epsilon}^p \ldots\ldots\ldots\ldots\ldots\ldots (4)$$

Where $\boldsymbol{u}$ is the plastic deformation which can be additively decomposed into elastic and plastic parts while the total strain rate ($\dot{\boldsymbol{\epsilon}}$) is obtained by differentiating equation 4 with respect to time

$$\dot{\boldsymbol{\epsilon}} = \dot{\boldsymbol{\epsilon}}^e + \dot{\boldsymbol{\epsilon}}^p \ldots\ldots\ldots\ldots\ldots\ldots\ldots (5)$$

This strain split gives the practical representation of deformation observed in confined compression enabling proper description of unloading and path-dependency (Grassal et al. 2011)

Hence, equation 1 can be rewritten as:

$$\boldsymbol{\sigma} = \boldsymbol{D^e}: (\boldsymbol{\epsilon} - \boldsymbol{\epsilon^p}) \ldots\ldots\ldots\ldots (6)$$

The plastic strain rate in equation 5 can be determined from the plastic flow rule as:

$$\dot{\epsilon}^p = \dot{\lambda}\boldsymbol{m} \ldots\ldots\ldots\ldots\ldots\ldots\ldots\ldots (6.1)$$

(Lubliner, 2008; Grassl and Jirasek, 2006; Belytschko et al. 2014; Hashiguchi, 2014 Kim, 2015)

2.1.2 Yield functions

The yield function that binds all possible stress states is expressed as:

$$f(\boldsymbol{\sigma}) \leq 0 \ldots\ldots\ldots\ldots\ldots\ldots\ldots\ldots\ldots (7)$$

$$\boldsymbol{\sigma} = \bar{\boldsymbol{\sigma}} - \boldsymbol{\sigma}_y(\bar{\boldsymbol{\varepsilon}}) \ldots\ldots\ldots\ldots\ldots\ldots\ldots\ldots (7.1)$$

With equation (7.1) for Von Mises yield criterion and equation (7.2) for Drucker-Prager yield criterion

$$f(\boldsymbol{\sigma}) = q - \alpha p - k \ldots\ldots\ldots\ldots\ldots\ldots\ldots (7.2)$$

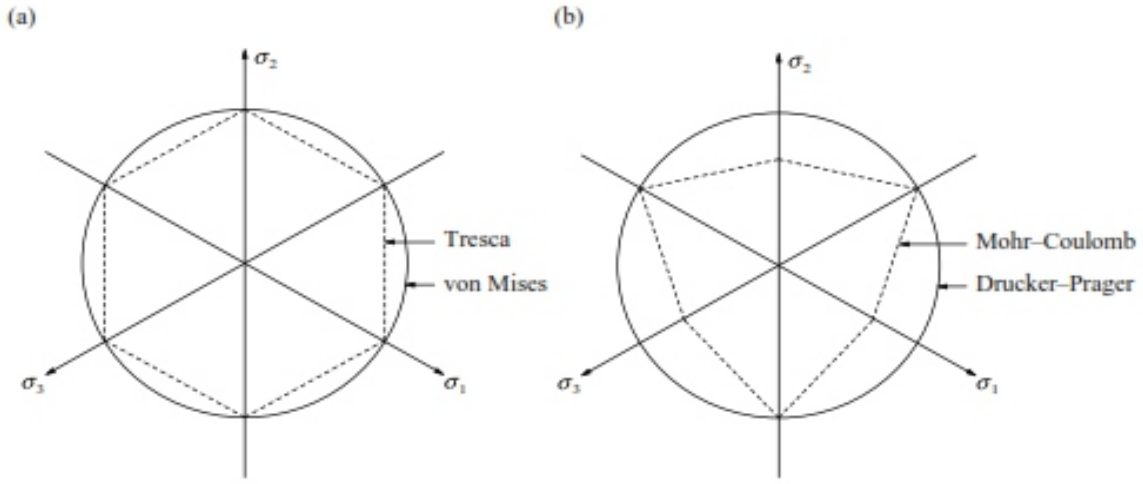

Figure 1.Representation of yield surfaces in the π- plane: (a) Tresca and von Mises; (b) Morhr-Coulomb and Drucker-Prager adapted from De Brost et al. 2012

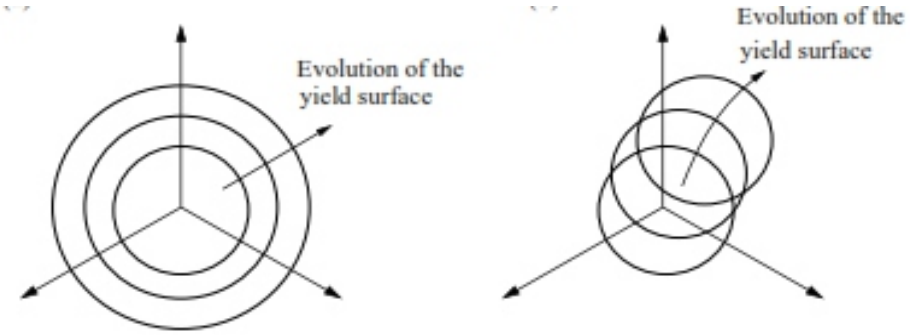

Figure 2.Different types of hardening (a) Isotropic hardening b) Kinematic hardening adapted from De Brost et al. 2012

However, for yield functions that include isotropic and kinematic hardening, the expression in equation (7.3) is adopted.

$$f = f(\boldsymbol{\sigma}, \boldsymbol{K}) \ldots\ldots\ldots\ldots\ldots\ldots\ldots\ldots (7.3)$$

Now for elastic deformation the stress state lies inside the yield contour and for such situations, the inequality holds.

$$f < 0 \ldots\ldots\ldots\ldots\ldots\ldots\ldots\ldots\ldots\ldots\ldots (8)$$

While for irreversible plastic deformations, the stress state is expected to lie on the yield contour for a brief period of time to allow for plastic deformation or plastic flow to occur; so that, plastic deformation takes place when the yield condition which is a function of stress (and in some cases hardening) disappears.

$$f = f(\boldsymbol{\sigma}) = 0 \ldots\ldots\ldots\ldots\ldots\ldots\ldots\ldots\ldots (9)$$

In rate form, the yield condition expressed as given in equation 10:

$$\dot{f} = 0 \ldots\ldots\ldots\ldots\ldots\ldots\ldots\ldots\ldots\ldots\ldots\ldots (10)$$

(Lubliner, 2008; Belytschko et al. 2014; Hashiguchi, 2014)

This rate form which is the derivative of the yield condition in equation 9 is also known as the consistency condition expressed as:

$$\dot{f} = \frac{\partial f}{\partial \boldsymbol{\sigma}} \cdot \dot{\boldsymbol{\sigma}} = \boldsymbol{n} \cdot \dot{\boldsymbol{\sigma}} = 0 \ldots\ldots\ldots\ldots (11)$$

this consistency condition $\dot{f} = 0$, is normal to the yield surface hence, the plastic flow direction ($\boldsymbol{m}$) is defined as the derivative of the plastic flow potential (Ψ) which is proportional to the normal to the yield surface f. That is:

$$\Psi \sim \mathrm{f} \ldots\ldots\ldots\ldots\ldots\ldots\ldots\ldots\ldots\ldots\ldots\ldots (12)$$

Hence,

$$\boldsymbol{m} = \frac{\partial \Psi}{\partial \boldsymbol{\sigma}} \ldots\ldots\ldots\ldots\ldots\ldots\ldots\ldots\ldots\ldots\ldots (13)$$

So that for an associated or normality flow rule, the choice of plastic potential should be such that the potential function (Ψ) has the same value as the yield function (f) that is:

$$\Psi = \mathrm{f} \ldots\ldots\ldots\ldots\ldots\ldots\ldots\ldots\ldots\ldots\ldots (14)$$

The benefit of this associative or normality flow rule is that the tangential stress strain relation of equation 2 becomes symmetric. From equations 11 and 12 plastic flow direction ($\boldsymbol{m}$) is co-linear with the gradient of the yield surface ($\boldsymbol{n}$) hence, the plastic flow direction can equally be expressed as:

$$\boldsymbol{m} = \gamma \boldsymbol{n} \ldots\ldots\ldots\ldots\ldots\ldots\ldots\ldots\ldots\ldots\ldots (15)$$

From Equations 6, 11 and 15, the plastic strain rate can also be written as:

$$\dot{\epsilon}^p = \dot{\lambda} \boldsymbol{n} \ldots\ldots\ldots\ldots\ldots\ldots\ldots\ldots\ldots\ldots\ldots (16) \ or$$

$$\dot{\epsilon}^p = \dot{\lambda} \frac{\partial f}{\partial \boldsymbol{\sigma}} \ldots\ldots\ldots\ldots\ldots\ldots\ldots\ldots\ldots\ldots\ldots (17)$$

For a non-associated plastic flow, the flow potential g does not correspond to the yield function (i.e. $\mathrm{g} \neq \mathrm{f}$) and the plastic flow direction is expressed as:

$$\boldsymbol{m} = \frac{\partial g}{\partial \boldsymbol{\sigma}} \ldots\ldots\ldots\ldots\ldots\ldots\ldots\ldots\ldots\ldots\ldots (18)$$

Hence, the plastic strain or flow rule ($\dot{\epsilon}^p$) becomes as expressed in equation (19). This expression allows for accurate modelling of volumetric expansion of frictional material such as concrete when subjected to shear deformations and also where the influence of hydrostatic pressure cannot be neglected.

$$\dot{\epsilon}^p = \dot{\lambda} \frac{\partial g}{\partial \boldsymbol{\sigma}} \ldots\ldots\ldots\ldots\ldots\ldots\ldots\ldots\ldots\ldots\ldots (19)$$

(Grassl and Jirasek 2006; Grassl et al. 2011; Belytschko et al. 2014; Xatto et al, 2014)

2.1.3Damage Mechanics Principles

The main structure of the constitutive models for damage is expressed as:

$$\boldsymbol{\sigma} = \boldsymbol{D}^{s}: \boldsymbol{\epsilon} \ldots\ldots\ldots\ldots\ldots\ldots\ldots\ldots\ldots\ldots\ldots (20)$$

$$\boldsymbol{D}^{s} = (1-\omega)\boldsymbol{D}^{e} \ldots\ldots\ldots\ldots\ldots\ldots\ldots\ldots\ldots (21)$$

Where $\omega -$ being the scalar valued internal damage variable whose magnitude increases progressively from zero to one as damage progresses to the absolute stage. It indicates how much of the system is still undamaged. The nominal stress in equation 20 in the spirit of damage mechanics can be rewritten as expressed in equation 22

$$\boldsymbol{\sigma} = (1-\omega)\widehat{\boldsymbol{\sigma}} \ldots\ldots\ldots\ldots\ldots\ldots\ldots\ldots\ldots\ldots (22)$$

Where $\widehat{\boldsymbol{\sigma}} -$ is the effective stress tensor expressed as:

$$\widehat{\boldsymbol{\sigma}} = \boldsymbol{D}^{e}: \boldsymbol{\epsilon} \ldots\ldots\ldots\ldots\ldots\ldots\ldots\ldots\ldots\ldots\ldots\ldots (23)$$

Equation 23 is differentiated with time to give the rate form as expressed in equation 23.1

$$\dot{\widehat{\boldsymbol{\sigma}}} = \boldsymbol{D}^{e}: (\dot{\boldsymbol{\epsilon}} - \dot{\boldsymbol{\epsilon}^{p}}) \ldots\ldots\ldots\ldots\ldots\ldots\ldots\ldots\ldots (23.1)$$

(Zhang and Cai, 2010; De Brost et al. 2012).

With the effective stress ($\widehat{\boldsymbol{\sigma}}$) used in the undamaged part of concrete between voids and micro-cracks; considering equations 20 to 23.1, the general expression for the stress stain relation is given as:

$$\boldsymbol{\sigma} = (1-\omega)\widehat{\boldsymbol{\sigma}} = (1-\omega)\boldsymbol{D}^{e}: (\boldsymbol{\epsilon} - \boldsymbol{\epsilon}^{p}) \ldots\ldots (24)$$

Equation 24 has a history dependence integrated via loading - unloading condition which depends on the following Kuhn-Tucker criterion:

$$f \leq 0; \qquad \dot{\lambda} \geq 0; \qquad \dot{\lambda} f = 0 \ldots\ldots (25)$$

For plastic loading, $\dot{\lambda} > 0$ this indicates that the stress state is on the yield surface that is $f = 0$ or $\dot{f} = 0$. For elastic loading on the other hand $\dot{\lambda} = 0$ with $f < 0$

The loading function thus expressed as in equation (26):

$$f(\hat{\epsilon}, k) = \hat{\epsilon} - k \ldots\ldots\ldots\ldots\ldots (26)$$

must equal zero upon damage growth and the evolution law which governs the growth of damage is expressed as:

$$\omega = \omega(k) \ldots\ldots\ldots\ldots\ldots\ldots\ldots\ldots\ldots\ldots (27)$$

(Grassl and Jirasek 2006; De Brost et al. 2012; Belytschko et al. 2014; Hashiguchi 2014)

3.0 Method and Materials

3.1 Combined Damage and Plasticity Models

Coupled plastic and damage models (which involve combining stress based plasticity with strain based damage models) for modelling concrete subjected to triaxial stress states have been proposed in literature (Janson et al. 2006; Grassl et al. 2011). The first two models discussed here have been studied with emphasis on local uniqueness condition Grassl and Jirasek 2006; while the last model (i.e. a coupled triaxial constitutive plastic damage model) is discussed in the context of continuum thermodynamics where by coupling of the dissipation mechanism of elastic-plastic behaviour and elastic damage was examined. (Salari et al. 2014). The models thus discussed are as follows:

a. Stress-based plasticity formulated in the effective stress space – which is the undamaged space.

Here the effective stress concept at the micro-level is defined as the force (F) transmitted by the concrete that is still intact, divided by the area (A) of the undamaged concrete expressed as:

$$\hat{\boldsymbol{\sigma}} = {}^{F}/_{A} = \frac{(1-\omega)\boldsymbol{E}A_0\epsilon}{A} \quad \ldots\ldots\ldots\ldots\ldots\ldots\ldots (28)$$

b. Plasticity formulated in the nominal stress space – that is the damaged space.

Here the nominal stress at the macro-level is given by force (F) divided by the original area (A_0) expressed as:

$$\sigma = {}^{F}/_{A_0} = (1-\omega)\boldsymbol{E}\boldsymbol{\epsilon} \ldots\ldots\ldots\ldots\ldots\ldots\ldots\ldots\ldots (29)$$

From equations 28 and 29 the following identity is observed

$$A = (1-\omega)A_0 \ldots\ldots\ldots\ldots\ldots\ldots\ldots\ldots\ldots\ldots\ldots (30)$$

Hence the effective stress of equation 28 can be further expressed as:

$$\hat{\boldsymbol{\sigma}} = \boldsymbol{E}:\boldsymbol{\epsilon} \ldots\ldots\ldots\ldots\ldots\ldots\ldots\ldots\ldots\ldots\ldots\ldots (31)$$

c. Stress-based plasticity is formulated in the effective stress space to model the dynamic behaviour of concrete.

d. The damage-plasticity model formulated in the framework of continuum thermodynamics

Here the Durker-Prager yield function for plastic loading is coupled with damage model where the scalar damage variable is incorporated into the plastic yield function via effective stress.

(Zhang and Cai, 2010; De Brost et al. 2012; Grassl and Jirasek 2006).

3.1 Stress-based Plasticity Formulated in the Effective Stress Space (undamaged space).

Here plasticity models determined using effective stress ($\hat{\boldsymbol{\sigma}}$) are merged with damage models based on total or plastic strain ($\boldsymbol{\epsilon}^p$). For this particular combination, the plastic part is based on the following plasticity theory:

1. Yield function (f_p) is expressed as:

$$f(\overline{\boldsymbol{\sigma}}, k_p) = \tilde{\boldsymbol{\sigma}}(\overline{\boldsymbol{\sigma}}) - \boldsymbol{\sigma}_y(k_p)) = 0 \ldots\ldots\ldots\ldots\ldots\ldots\ldots (32)$$

In equation (32), the internal variable k has been introduced into the yield function to make up for hardening and softening through the introduction of hardening and softening parameters.

2. Plastic flow rule expressed as:

$$\dot{\epsilon}^p = \dot{\lambda}\frac{\partial g_p}{\partial \overline{\boldsymbol{\sigma}}}(\overline{\boldsymbol{\sigma}}, k_p) \ldots\ldots\ldots\ldots\ldots\ldots\ldots\ldots\ldots\ldots\ldots\ldots\ldots\ldots (33)$$

3. With the evolution equation for the kinematic hardening internal variable expressed as:

$$\dot{k_p} = \dot{\lambda} k_p(\overline{\boldsymbol{\sigma}}, k_p) \ldots\ldots\ldots\ldots\ldots\ldots\ldots\ldots\ldots\ldots\ldots\ldots\ldots (34)$$

4. Loading-unloading conditions:

$$\dot{f_p} \leq 0; \;\; \dot{\lambda} \geq 0; \;\; \dot{\lambda}\,\dot{f_p} = 0 \ldots\ldots\ldots\ldots\ldots\ldots\ldots (35)$$

While the damage part is expressed based on the following damage models:

1. Loading and unloading damage function expressed as:

$$f_d\left(\boldsymbol{\epsilon}, \; \boldsymbol{\epsilon}_p, \; k_d\right) = \tilde{\boldsymbol{\epsilon}}(\boldsymbol{\epsilon}, \boldsymbol{\epsilon}_p) - k_d \ldots\ldots\ldots\ldots\ldots\ldots\ldots\ldots\ldots\ldots\ldots\ldots (36)$$

2. Evolution law governing damage growth given as:

$$\omega = g_d(k_d) \ldots\ldots\ldots\ldots\ldots\ldots\ldots\ldots\ldots\ldots\ldots\ldots\ldots\ldots\ldots (37)$$

3. Loading-unloading conditions:

$$\dot{f_d} \leq 0; \quad \dot{k_d} \geq 0; \quad \dot{f_d}\dot{k_d} = 0 \ldots\ldots\ldots\ldots\ldots (38)$$

For both plastic and damage models, $\dot{f_p} = 0$ and $\dot{f_d} = 0$ are the necessary conditions to satisfy where the damage variable is incorporated into the plastic yield function via effective stress. Differentiating equation 32 with time and taking advantage of equations 33 and 34; the rate form of the yield function becomes expressed as given in equation 39. Where H_p is the plastic modulus which is positive for hardening and negative for softening.

$$\dot{f_p} = \frac{\partial f_p}{\partial \overline{\boldsymbol{\sigma}}} : \dot{\overline{\boldsymbol{\sigma}}} + \frac{\partial f_p}{\partial k_p}\dot{k_p} = \frac{\partial f_p}{\partial \overline{\boldsymbol{\sigma}}}\boldsymbol{D^e} : \dot{\boldsymbol{\epsilon}} - \dot{\lambda}\left(\frac{\partial f_p}{\partial \overline{\boldsymbol{\sigma}}} : \boldsymbol{D^e} : \frac{\partial g_p}{\partial \overline{\boldsymbol{\sigma}}} + H_p k_d\right) \ldots\ldots\ldots\ldots (39)$$

$$\frac{\partial f_p}{\partial \overline{\boldsymbol{\sigma}}} : \boldsymbol{D^e} : \frac{\partial g_p}{\partial \overline{\boldsymbol{\sigma}}} + H_p k_d > 0 \ldots\ldots\ldots\ldots\ldots\ldots\ldots\ldots\ldots\ldots\ldots\ldots\ldots\ldots\ldots\ldots\ldots\ldots\ldots\ldots (39.1)$$

The study of this combined plastic and damage model focuses on the local uniqueness where it is possible to show that the expression in brackets have a unique solution for a few specified stain rate $\dot{\epsilon}$. However, if the expression in bracket is negative, no solution is believed to exist for those strain rates that result in the left part of the expression in the bracket becoming negative. This is equally so when the expression in bracket equals zero. Implying that, the condition for local uniqueness is such that equation 39.1 be greater than zero and must be complied with for all possible conditions of the material else, some strain histories will generate equivalent stress histories that cannot be uniquely verified by the model equations (Grassl and Jirasek, 2006). Reference should be made to Grassl and Jirasek, (2006) for a more detailed discussion.

(De Brost et al, 2012; Xotta, 2014).

3.2 Plasticity Formulated in the Nominal Stress Space (damaged).

Here the plastic part is based on nominal stress ($\boldsymbol{\sigma}$) and the basic governing equations are as follows:

Yield function (f_p) is expressed as:

$$f(\boldsymbol{\sigma}, k_p) = \tilde{\boldsymbol{\sigma}}(\boldsymbol{\sigma}) - \boldsymbol{\sigma}_y(k_p)) = 0 \dots \dots \dots \dots \dots \dots \dots \dots \dots \dots \dots \dots \dots \dots \dots \dots \dots .. \dots (40)$$

2. Plastic flow rule expressed as:

$$\dot{\epsilon}^p = \dot{\lambda}\frac{\partial g_p}{\partial \boldsymbol{\sigma}}(\boldsymbol{\sigma}, k_p) \dots \dots \dots \dots \dots \quad \dots \dots \dots \dots \dots . \dots \dots \dots \dots \dots \dots \dots \dots \dots \dots \dots .. \dots \dots (41)$$

3. The evolution equation for the kinematic hardening internal variable expressed as:

$$\dot{k_p} = \dot{\lambda} k_p(\boldsymbol{\sigma}, k_p) \dots \dots \dots \dots \dots \dots \dots \dots . \dots \dots \dots \dots \dots \dots \dots \dots \dots \dots \dots \dots (42)$$

4. Loading-unloading conditions:

$$f \leq 0; \qquad \dot{k} \geq 0; \qquad f\dot{k} = 0 \dots \dots \dots \dots \dots \dots \dots \dots \dots \dots \dots \dots \dots \dots .. \dots \dots .. (43)$$

The damage models remain unchanged. Again, for detailed explanation of this model, reference should be made to Grassl and Jirasek, (2006) where again the focus is on study of the following three conditions of local uniqueness that is:

$$(1-\omega)\frac{\partial f_p}{\partial \boldsymbol{\sigma}} : \boldsymbol{D}^e : \frac{\partial g_p}{\partial \boldsymbol{\sigma}} + H_p k_d > 0 \dots \dots \dots \dots \dots \dots \dots \dots \dots \dots \dots \dots . \dots \dots \dots . (44)$$

$$1 > 0 \quad \dots \dots \dots \dots \dots \dots \dots \dots \dots \dots \dots \dots \dots \dots \dots .; \dots \dots \dots \dots \dots \dots \dots \dots \dots \dots \dots .. \dots \dots . (45)$$

$$(1-\omega)\frac{\partial f_p}{\partial \boldsymbol{\sigma}} : \boldsymbol{D}^e : \frac{\partial g_p}{\partial \boldsymbol{\sigma}} + H_p k_d > \frac{\partial f_d}{\partial \boldsymbol{\epsilon}_p} : \frac{\partial g_p}{\partial \boldsymbol{\sigma}} \left(\frac{dg_p}{dk_d}\frac{\partial f_p}{\partial \boldsymbol{\sigma}} : \bar{\boldsymbol{\sigma}}\right) \quad \dots \dots \dots \dots \dots \dots . (46)$$

For the models based on effective stress, no additional restriction on model parameters is necessary to ensure local uniqueness is satisfied. For the models based on nominal stress on the other hand, additional restriction on hardening is required to satisfy local uniqueness which presented difficulties especially in the modelling of uniaxial and low-confined compression where softening has been observed in the experimental findings (Grassl and Jirasek, 2006).

3.3 Stressbased plasticity formulated in the effective stress space to model the dynamic behaviour of concrete.

A coupled damage-plasticity model with the objective of providing computationally and well-organised accurate description of the behaviour of concrete subjected to dynamic loading is presented by Grassl et al. (2011) as given in equation (47).

$$\boldsymbol{\sigma} = (1-\omega_t)\bar{\boldsymbol{\sigma}}_t + (1-\omega_c)\bar{\boldsymbol{\sigma}}_c \dots \dots \dots \dots \dots \dots \dots \dots (47)$$

Where $\bar{\boldsymbol{\sigma}}_t$ and $\bar{\boldsymbol{\sigma}}_c$ are derived from principal effective stress as:

$$\bar{\boldsymbol{\sigma}}_{pt} = \langle \bar{\boldsymbol{\sigma}}_p \rangle_+ \; and \; \bar{\boldsymbol{\sigma}}_{pc} = \langle \bar{\boldsymbol{\sigma}}_p \rangle_- \dots \dots \dots \dots \dots \dots \dots \dots (48)$$

To make a distinction between the tensile and compressive stress states, a scalar measure α_c is defined expressed as:

$$\alpha_c = \sum_i \frac{\langle \bar{\boldsymbol{\sigma}}_{pi} \rangle_- \left(\langle \bar{\boldsymbol{\sigma}}_{pi} \rangle_+ + \langle \bar{\boldsymbol{\sigma}}_{pi} \rangle_-\right)}{//\bar{\boldsymbol{\sigma}}_{\boldsymbol{p}}//^2} \dots \dots \dots \dots \dots \dots \dots \dots (49)$$

The above parameter α_c varies from 0 to 1.

This model is again based on a stress-based plasticity formulated in the effective stress space.

$$\overline{\boldsymbol{\sigma}} = \boldsymbol{D}^{\boldsymbol{e}} : (\boldsymbol{\epsilon} - \boldsymbol{\epsilon}^{\boldsymbol{p}}) \ldots\ldots\ldots\ldots\ldots\ldots\ldots\ldots\ldots\ldots\ldots\ldots\ldots\ldots\ldots\ldots\ldots (50)$$

Here the damage model which describes the complicated strength envelope of concrete to dynamic load is set up with elastic and plastic strain measures that differentiate between tensile and compressive stress states. The hardening in the post-peak regime of the stress strain curve (see Figure 3) facilitates modelling of the strain rate dependence of concrete strength by slowing down the onset of damage.

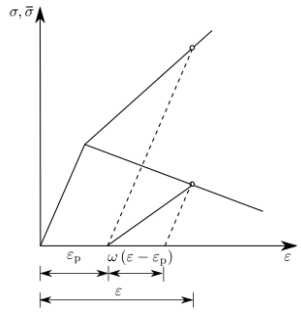

Figure 3.Geometrical meaning of the inelastic stain $(\boldsymbol{\epsilon}_i)$ for the combined damage-plasticity model. The inelastic strain is composed of reversible $\omega(\boldsymbol{\epsilon} - \boldsymbol{\epsilon}^{\boldsymbol{p}})$ and irreversible $(\boldsymbol{\epsilon}^{\boldsymbol{p}})$ parts. The dashed lines represent elastic unloading with the same stiffness as the initial elastic loading. Adapted from Grassl et al. 2011

odel equations

illustrated in
dependence of

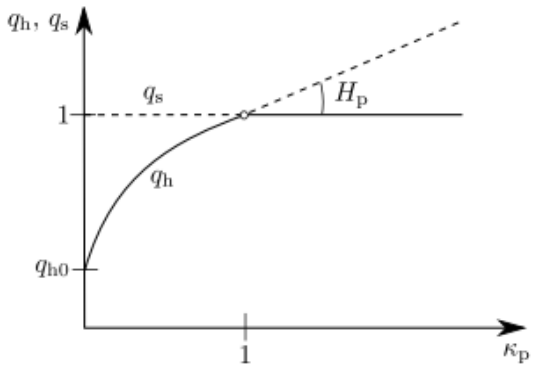

Figure 4.The two hardening laws $\boldsymbol{q}_h$ (solid line) and $\boldsymbol{q}_s$ (dashed line); adapted from Grassl et al. 2011.

3. Loading-unloading conditions:

$$f_p \leq 0; \quad \dot{\lambda} \geq 0; \quad \dot{\lambda}\, f_p = 0 \ldots\ldots\ldots\ldots\ldots\ldots\ldots\ldots\ldots (53)$$

While the damaged part of this model is related to elastic and plastic strain measures. So that the state of stress under pure tension is:

$$\bar{\boldsymbol{\sigma}}_t = \bar{\boldsymbol{\sigma}};\ \ \bar{\boldsymbol{\sigma}}_c = 0;\ \ and\ \omega_t = \omega \ldots\ldots\ldots\ldots\ldots\ldots\ldots\ldots\ldots\ldots (54)$$

Hence equation 47 can be written as:

$$\boldsymbol{\sigma} = (1-\omega)\bar{\boldsymbol{\sigma}} = (1-\omega)\boldsymbol{D}^{\boldsymbol{e}}\!:(\boldsymbol{\epsilon}-\boldsymbol{\epsilon}^{\boldsymbol{p}}) \ldots\ldots\ldots\ldots\ldots\ldots\ldots (55)$$

$$\boldsymbol{\sigma} = \boldsymbol{D}^{\boldsymbol{e}}\!:(\boldsymbol{\epsilon}-(\boldsymbol{\epsilon}^{\boldsymbol{p}}+\omega\,(\boldsymbol{\epsilon}-\boldsymbol{\epsilon}^{\boldsymbol{p}}))) = \boldsymbol{D}^{\boldsymbol{e}}\!:(\boldsymbol{\epsilon}-\boldsymbol{\epsilon}^{\boldsymbol{p}}) \ldots\ldots\ldots (56)$$

Where the inelastic strain $(\boldsymbol{\epsilon}_i)$ expressed as given in equation (57) is subtracted from the elastic strain (see Figure 3)

$$\boldsymbol{\epsilon}_i = \boldsymbol{\epsilon}^{\boldsymbol{p}} + \omega\,(\boldsymbol{\epsilon}-\boldsymbol{\epsilon}^{\boldsymbol{p}}) \ldots\ldots\ldots\ldots\ldots\ldots\ldots\ldots\ldots\ldots\ldots\ldots\ldots (57)$$

Based on the plastic and elastic strain measures, the damage parameter is obtined using history variables. The elastic strian is refered to here as the equivalent strain $\bar{\boldsymbol{\epsilon}}$ and it is selected such that at the effective stress state commencement of damage it complies with the Menetrey and Willam (1995) yield criterion (in which the yield surface in which the plastic part is established) (Grassl et al. 2011).

1. The equivalent damage enveloped is thus expressed as:

$$\frac{2}{3}\frac{\bar{\rho}^2}{{f_c}^2} + q_d m_0\left(\frac{\bar{\rho}}{\sqrt{6}f_c}r(cos\,\bar{\theta}) + \frac{\bar{\sigma}_v}{f_c}\right) - {q_d}^2 = 0 \ldots\ldots\ldots\ldots\ldots\ldots (58)$$

Where the hardening variable q_d is proportional to the effective stress in tension and compresion i.e. $q_d = \frac{\bar{\sigma}_t}{f_t};\ \ q_d = \frac{\bar{\sigma}_c}{f_c};$ hence, the equivalent strain $\bar{\boldsymbol{\epsilon}}$ is expressed as:

$$\bar{\boldsymbol{\epsilon}} = \frac{f_t}{E}q_d \ldots\ldots\ldots\ldots\ldots\ldots\ldots\ldots\ldots (59)$$

2. For this model, we have two damage loading function, one for tension and another for compression

$$f_{dt} = \frac{1}{\alpha_r}\,\bar{\boldsymbol{\epsilon}} - K_{dt} \ldots\ldots\ldots\ldots\ldots\ldots\ldots\ldots\ldots\ldots\ldots\ldots (60)$$

$$f_{dc} = \frac{\alpha_c}{\alpha_r}\,\bar{\boldsymbol{\epsilon}} - K_{dc} \ldots\ldots\ldots\ldots\ldots\ldots\ldots\ldots\ldots\ldots\ldots\ldots (61)$$

where the variable α_r facilites modelling of the strain rate dependence of concrete such that as α_r increases in value, so does the commencement of damage slows down and therewith, strength. While α_c facilitates modelling the different strain rate dependence of concrete in tension and compression (Grassl et al. 2011).

Both loading funcitons in equations 60 and 61 control the evolution of the following six damage history loading variables i.e. $K_{dt},\ K_{dc}, K_{d1t}, K_{d1c}, K_{d2t}, K_{d2c}$ used in evaluating the damage parameters ω_t and ω_c which are dependent on the type of softening been modelled (see bilinear softening model in fig 5).

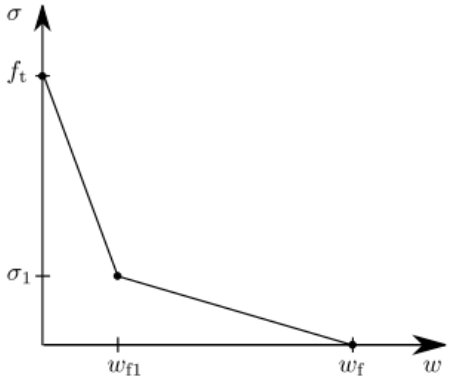

Figure 5.Bilinear stress strain curve adabpted from Grassl 2011.

3. Loading and unloading condition in tension and compression are expressed as follows:

$$f_{dt} \leq 0; \quad \dot{k}_{dt} \geq 0; \quad \dot{k}_{dt} f_{dt} = 0 \ldots\ldots\ldots\ldots\ldots\ldots \quad (62)$$

$$f_{dc} \leq 0; \quad \dot{k}_{dc} \geq 0; \quad \dot{k}_{dc} f_{dc} = 0 \ldots\ldots\ldots\ldots\ldots\ldots \quad (63)$$

After the commencement of damage, only the plastic strains are considered. Hence, the six damage history are thus defined as:

$$\dot{k}_{d1t} = \begin{cases} \frac{1}{x_s \alpha_r} \dot{k}_p & if\ \dot{k}_{dt} > 0 \wedge k_{dt} > \epsilon_0 \ldots\ldots\ldots\ldots\ldots\ldots\ldots\ldots\ldots\ldots \quad (64) \\ & if\ \dot{k}_{dt} = 0 \vee k_{dt} < \epsilon_0 \ldots\ldots\ldots\ldots\ldots\ldots\ldots\ldots\ldots\ldots \quad (64) \end{cases}$$

$$\dot{k}_{d1c} = \begin{cases} \frac{\alpha_c}{x_s \alpha_r} \dot{k}_p & if\ \dot{k}_{dc} > 0 \wedge k_{dc} > \epsilon_0 \ldots\ldots\ldots\ldots\ldots \quad (65) \\ & if\ \dot{k}_{dc} = 0 \vee k_{dc} < \epsilon_0 \ldots\ldots\ldots\ldots \quad (65) \end{cases}$$

$$\dot{k}_{d2t} = \frac{\dot{k}_{dt}}{x_s} \ldots\ldots\ldots\ldots\ldots\ldots\ldots\ldots\ldots\ldots\ldots\ldots\ldots\ldots\ldots\ldots \quad (66)$$

$$\dot{k}_{d2c} = \frac{\dot{k}_{dc}}{x_s} \ldots\ldots\ldots\ldots\ldots\ldots\ldots\ldots\ldots\ldots\ldots\ldots\ldots\ldots\ldots\ldots \quad (67)$$

The parameter x_s is the ductility measure which is used in manipulating the ratio of fracture energies in tension G_{ft} as well as in compression G_{fc}.

The above coupled damage-plasticity models showed an overall agreement with experimental results of Gopalaratnam and Shah (1985); Karsan and Jirasan (1969); Kupfer et al. (1969); Caner and Bazant (1996); cited in Grassl et al. 2011.

3.4 The damageplasticity model formulated in the framework of continuum thermodynamics

The coupled triaxial constitutive plastic damage model which describes tensile damage was put together in the context of continuum thermodynamics with the aid of internal variables where the Helmholtz free energy function ($\psi = \psi(\epsilon^e, k, D)$ was adopted; to ensure that the second principles of thermodynamics

is complied with, the local Clausius-Duhem's inequality stresses that the reduced dissipation inequality holds as:

$$\sigma : \dot{\varepsilon} - \dot{\psi} \geq \ 0 \ldots\ldots\ldots\ldots\ldots\ldots\ldots\ldots\ldots\ldots\ldots\ldots..\ldots.\ldots\ldots\ldots.(68)$$

(Xotta et al. 2014; Salari et al. 2004)

Where:

The Helmholtz free energy function (ψ) is additively decomposed into the elastic and plastic parts expressed as:

$$\psi = \psi^e(\epsilon^e, D) \ + \ \psi^P(\epsilon^P, D) \ \ldots\ldots\ldots\ldots\ldots\ldots\ldots\ldots..\ldots.(68.1)$$

And the local Clausius-Duhem's inequality is given as:

$$\left(\boldsymbol{\sigma} - \frac{\partial\psi^e}{\partial\epsilon^e}\right)\dot{\epsilon} + \frac{\partial\psi^e}{\partial\boldsymbol{\sigma}^e}\dot{\epsilon}^p - \frac{\partial\psi^p}{\partial k}\dot{k} - \frac{\partial\psi}{\partial D}D \geq 0 \ldots\ldots\ldots\ldots\ldots.(69)$$

obtained by substituting the derivative of eqn. 68.1 into eqn. 68; where equation (68.1) has been additively decomposed into the elastic and plastic components. The constitutive expression as well as the thermodynamic conjugate forces for damage and plasticity is as follows:

$$\left.\begin{aligned} \boldsymbol{\sigma} &= \frac{\partial\psi^e}{\partial\epsilon^e} \\ Y &= -\frac{\partial\psi}{\partial D} \\ K &= -\frac{\partial\psi^P}{\partial D} \end{aligned}\right\} \qquad \ldots\ldots\ldots\ldots\ldots.(69.1)$$

This damage plasticity model formulated on the framework of thermodynamics, takes on an isotropic elastic damage characterised by a single scalar damage variable which changes under an expansive volumetric strain. The Drucker-Prager pressure-sensitive yield function is used to explain the plastic behaviour while a non-associated flow rule used to manage inelastic dilatancy. Here, damage is established in the plastic loading function by way of effective stress and represented by a scalar damage variable (D) which is believed to preserve the isotropic elastic behaviour as the damage variable changes under volumetric expansion; the plastic parts are however, based on the following basic models

1. Plasticity loading functions f^p expressed as

$$f^p \ = f^p\ (\boldsymbol{\sigma}, K; D) \ldots\ldots\ldots\ldots\ldots.(70)$$

2. A pressure sensitive yield function expressed as:

$$f^p \ = (\boldsymbol{\sigma}, \bar{e}^p; D) = \alpha I_1 + \sqrt{J_2} - (1 - D)k \ \ldots\ldots\ldots\ldots\ldots\ldots\ldots(71)$$

Dividing equation (71) by $(1 - D)$ gives the effect of damage on the cohesive strength.

The consistency condition to satisfy for plasticity is:

$$\dot{f}^p = \frac{\partial f^p}{\partial \boldsymbol{\sigma}} : \dot{\boldsymbol{\sigma}} + \frac{\partial f^p}{\partial \bar{e}^p}\dot{\bar{e}}^p + \frac{\partial f^p}{\partial D}\dot{D} = 0 \quad \ldots\ldots\ldots\ldots\ldots\ldots\ldots (72)$$

Here, it has been assumed that plastic hardening relies on the equivalent effective deviatoric plastic strain ($\bar{e}^p$) instead of the total plastic strain (e^p). Hence, the plastic strain rate is expressed as:

$$\dot{\bar{e}}^p = \sqrt{\frac{2}{3} d\bar{e}^p : d\bar{e}^p} \quad \ldots\ldots\ldots\ldots\ldots\ldots\ldots\ldots\ldots\ldots\ldots\ldots (72.1)$$

The volumetric part of the plastic strain on the other hand is employed in establishing softening instead of hardening.

3. Plastic flow rule for plasticity is expressed as:

$$\dot{\epsilon}^p = \dot{\lambda}\frac{\partial g^d}{\partial \boldsymbol{\sigma}} \ldots\ldots\ldots\ldots\ldots\ldots\ldots\ldots\ldots\ldots\ldots\ldots\ldots\ldots\ldots\ldots (73)$$

Equation (73) is a non-associated flow rule which is used in regulating the inelastic dilatancy.

4. While the rate of change for internal variable is expressed as:

$$\dot{k} = \dot{\lambda}\frac{\partial g^p}{\partial K} \ldots\ldots\ldots\ldots\ldots\ldots\ldots\ldots\ldots\ldots\ldots\ldots\ldots\ldots\ldots\ldots (74)$$

$$\dot{D} = \dot{\mu}\frac{\partial g^d}{\partial Y} \ldots\ldots\ldots\ldots\ldots\ldots\ldots\ldots\ldots\ldots\ldots\ldots\ldots\ldots\ldots\ldots (75)$$

5. The potential function for plasticity (g^p) and damage (g^d) is expressed as:
$$g^p = g^p(\boldsymbol{\sigma}, K; D); \qquad g^d = g^d(Y; D) \ldots\ldots (75.1)$$

6. Loading-unloading conditions for the rate multipliers:
$$\dot{\lambda} \geq 0; \qquad \dot{\mu} \geq 0 \quad \ldots\ldots\ldots\ldots\ldots\ldots\ldots\ldots\ldots\ldots (76)$$

While the damage part is expressed based on the following damage models:

1. The energy-based damage function which describes damage initiation by the loading function (f^d) is expressed as:

$$f^d = f^d(Y_V; D) = Y_V - r(D) \ldots\ldots\ldots\ldots\ldots\ldots\ldots (77)$$

Where the volumetric part of the thermodynamic damage force that cause the evolution of damage representing energy demand is expressed as:

$$Y_V = \frac{1}{2}K^0\langle \epsilon^e{}_V \rangle^2 + c\int_v^{\epsilon^p{}_V} /\sigma_m/\langle d\epsilon^p{}_V \rangle \ldots\ldots\ldots\ldots\ldots\ldots (77.1)$$

And the energy resistance function is expressed as:

$$r(D) = r_0(1-D)^{p-1} \ldots\ldots\ldots\ldots\ldots\ldots\ldots\ldots\ldots\ldots\ldots\ldots (77.2)$$

Where r_0 is the modulus of resilience or the volumetric strain energy at peak stress as shown in Figure 6; p, the ratio of modulus of resistance (r_0) to the modulus of toughness (g_f) is expressed as:

$$p = \frac{r_0}{g_f} \ldots\ldots\ldots\ldots\ldots\ldots\ldots\ldots\ldots\ldots\ldots\ldots\ldots\ldots\ldots\ldots\ldots\ldots\ldots\ldots (77.3)$$

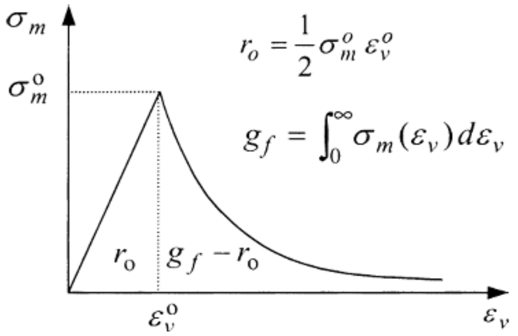

Figure 6.Uniaxial stress-strain curve of the damage model adapted from Salari et al. 2004

2. The consistency condition to satisfy for damage is:

$$\dot{f}^d = \frac{\partial f^d}{\partial Y_V}\dot{Y}_V + \frac{\partial f^d}{\partial D}\dot{D} = 0 \ldots\ldots\ldots\ldots\ldots\ldots\ldots\ldots\ldots\ldots\ldots\ldots\ldots\ldots\ldots\ldots\ldots\ldots\ldots (78)$$

3. The volumetric thermodynamic force $(\dot{Y}_V)$ is given as:

$$\dot{Y}_V = K^0\langle\epsilon^e{}_V\rangle \boldsymbol{I}{:}\,\dot{\epsilon} - 3\lambda\left(K^0\langle\epsilon^e{}_V\rangle\frac{\partial g^p}{\partial I_1} - c/\sigma_m/\langle\frac{\partial g^p}{\partial I_1}\rangle\right) \ldots\ldots\ldots\ldots\ldots\ldots\ldots\ldots (79)$$

Substituting equation 79 into equation 78 yields the second consistency condition expressed as:

$$-3R_d(K^0\langle\epsilon^e{}_V\rangle\frac{\partial g^p}{\partial I_1} - c/\sigma_m/\langle\frac{\partial g^p}{\partial I_1}\rangle)\lambda + \dot{D} - R_d K^0\langle\epsilon^e{}_V\rangle \boldsymbol{I}{:}\,\dot{\epsilon} = 0 \ldots\ldots (80)$$

With

$$R_d = \frac{\partial f^d}{\partial Y_V} / \frac{\partial f^d}{\partial D} \quad where\ R_d < 0 \ldots\ldots\ldots\ldots\ldots\ldots\ldots\ldots\ldots\ldots\ldots\ldots\ldots\ldots\ldots\ldots (81)$$

4. The equation for the plastic $\dot{\lambda}$ and damage $\dot{D}$ multipliers are expressed as follows:

$$\begin{bmatrix} A_{11} & A_{12} \\ A_{21} & A_{22} \end{bmatrix} \begin{bmatrix} \dot{\lambda} \\ \dot{D} \end{bmatrix} = \begin{bmatrix} B_1 \\ B_2 \end{bmatrix} \ with \begin{bmatrix} \dot{\lambda} \\ \dot{D} \end{bmatrix} = \frac{1}{A_{11}A_{22} - A_{12}A_{22}} \begin{bmatrix} A_{22} & -A_{12} \\ -A_{21} & A_{11} \end{bmatrix} \begin{bmatrix} B_1 \\ B_2 \end{bmatrix} - (82)$$

$$a)\ \dot{D} > 0 \quad if\ A_{11}B_2 - A_{21}B_1 > 0,$$

$$b)\ \dot{\lambda} > 0 \quad if\ A_{22}B_1 - A_{12}B_2 > 0.$$

This combined plastic and damage model has been widely studied by Xotta et al, (2014); Salari et al (2004) in more detail.

4.0 Results and Discussions

4.1 Damage Assessment of a Reinforced Concrete Beam under Uniformly Distributed Pressure Load using the Damage Plasticity Model

The damage-plasticity model discussed has been used to analyse the reinforced concrete beam subjected to a uniform pressure load of 2MPa. This three-dimensional finite element model consists of 3D deformable beam elements with material and geometric non-linearities for the steel rebar where damage plasticity model has been used to assess failure if any.

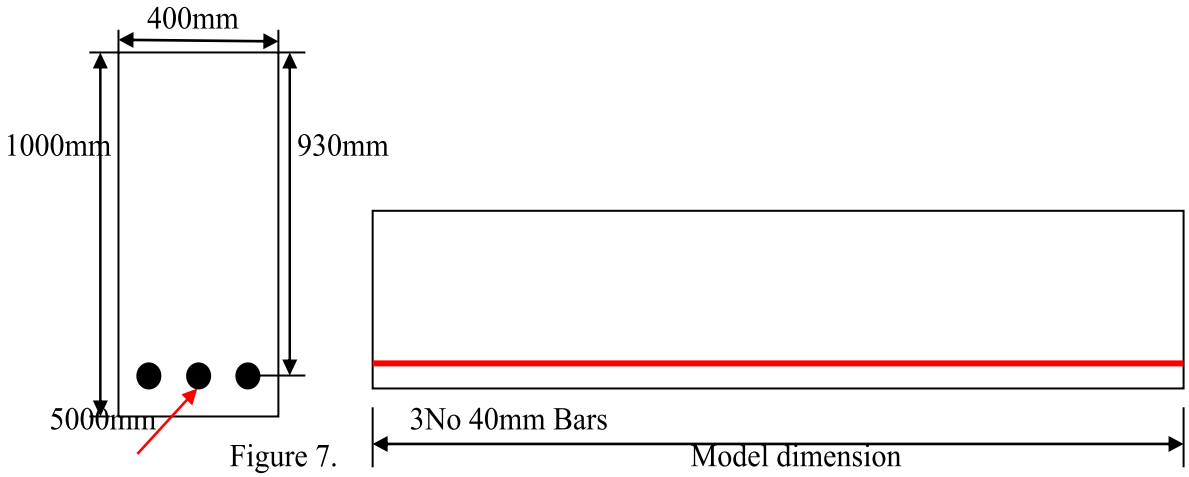

Figure 7.

Model dimension is 5000 x 400 x 1000; with boundary condition pinned at both ends.

The material parameters are as follows:

Concrete:

$$f_c{}' = 30MPa$$
$$v_c = 0.15$$
$$\rho = 2.4E-6\ Kg/mm^3$$

Steel:

$$A_s = 3770mm^2$$
$$f_y = 460MPa$$
$$v_s = 0.3$$

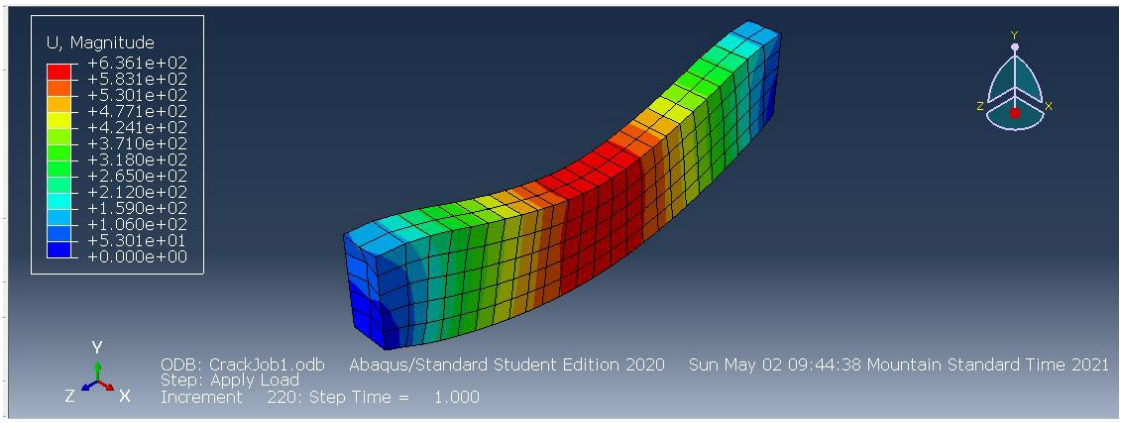

Figure 8.Deformed shape of beam subjected to a uniform pressure load of 2MPa

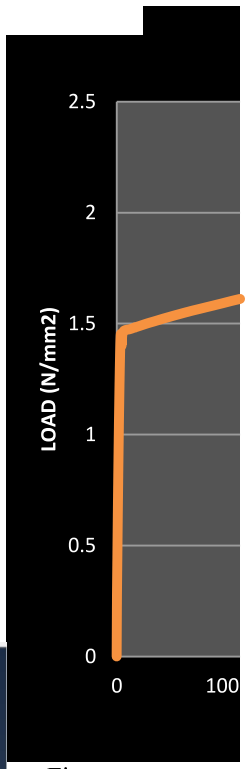

Figure 9.Load displacement curve of the beam under applied uniform

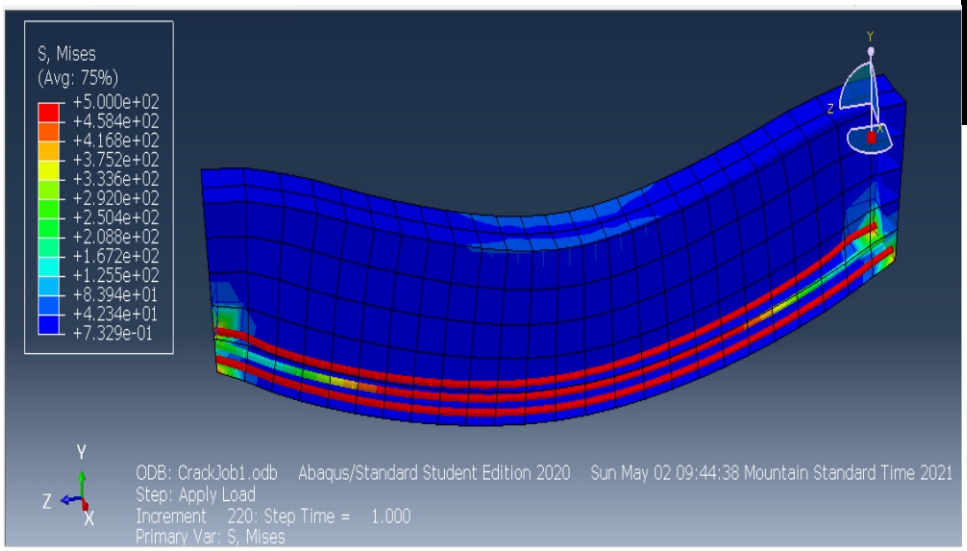

pressure load of 2MPa

Figure 10.Von Mises yield stress for the rebar.

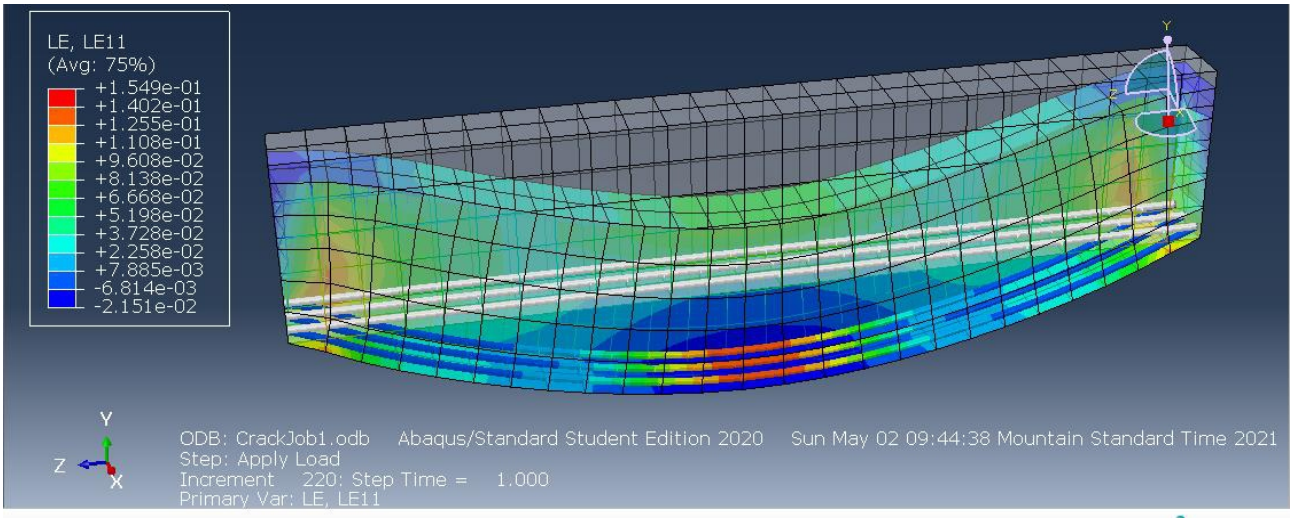

Figure 11.Deformed and undeformed shape of the beam

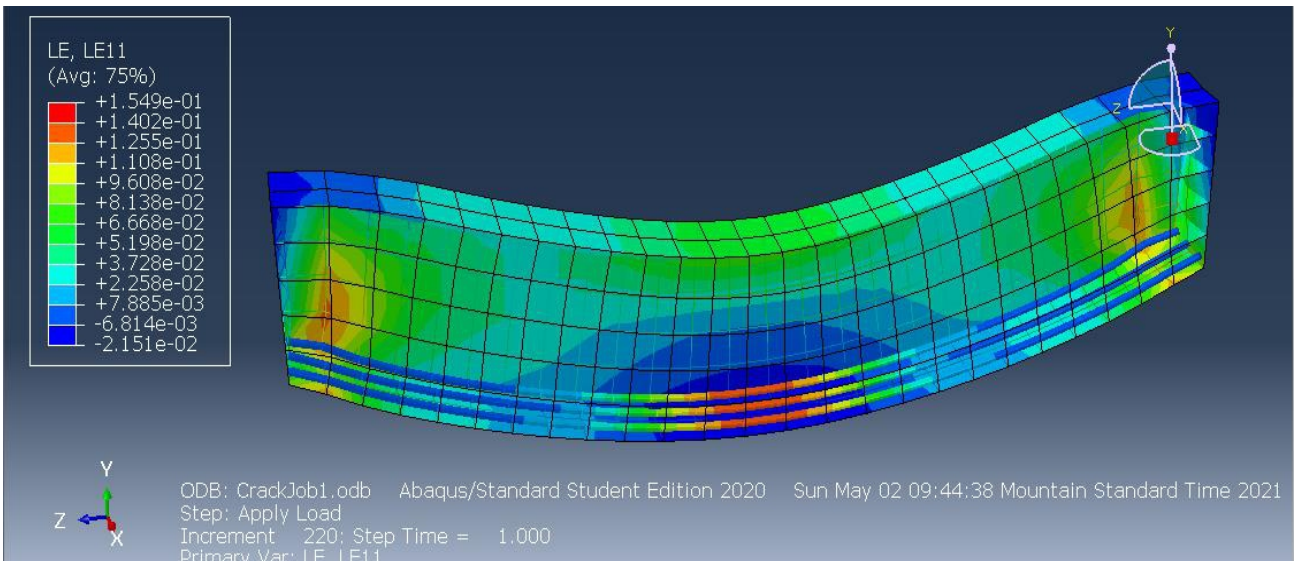

Figure 12.Deformed shape of the beam with the stress distribution pattern showing cracks at both ends of the beam

The Von Mises yield stress for rebar as shown in figure 10 shows that the steel has yielded excessively along the entire length on both ends of the beam. Also, from the deformed and undeformed shape of the damage plasticity model presented in figures 11 and 12, the strain (LE) in the horizontal direction (LE11) as well as the stress distribution patterns shows the presence of crack distribution at both ends of

the beam which increased in size as the tension in the beam increased under the applied loading. This shows the strength of the plastic damage model when assessing damage in concrete materials.

5.0 Conclusion and recommendation

Coupled plastic-damage models based on stress-based plasticity formulated in the effective stress space with a strain based damage model for modelling the non-linear mechanical behaviours of concrete have been examined. It has been observed from the present study that:

- Plastic-damage models that fall under this group have shown good agreement with a wider range of experimental results for proportional loading (i.e. loading with constant stress strain amplitude) as well as rate dependent loading.
- For non-proportional loading (i.e. when the stress stain amplitude varies with time) minor discrepancies were observed.
- Under three dimensional structural applications, its prediction was sufficiently accurate for beams under uniformly distributed loading.

Recommendations

Further investigation should be carried out to study the discrepancies observed between non-proportional loading and experimental results. Furthermore, plastic-damage models for modelling novel concrete based material such as fibre reinforced concrete, is still not well established. An improvement in these areas will be beneficial in ensuring accurate modelling of nonlinear mechanical behaviours in concrete and fibre reinforced augmented concrete structures to both proportional/non-proportional loadings as well as rate-dependent loading.

References

De Borst, R. Crisfileld, MAR Remmers, JJC & Verhrosel, CV. 2012. Non-linear Finite Element Analysis of Solid and Structures 2nd Edition. Johon Wiley and Sons Ltd. United Kingdom

Grassl , P. and Jirasek, M. 2006. Damage Plastic Model for Concrete Failure. International Journal of Solids and Structures , 43:. 7166-7196.

Belytschko, T. Liu, WK. Moran, B. and Elkhoday, KI. 2014. Nonlinear Finite Element for Continuua and Structures. Second Edition ed. West Sussex United Kingdom: John Wiley and Sons

Hashiguchi, K. 2014. Elastoplasticity Theory. 2nd Edition ed. Hannover Germany: Springer.

Grassl, P. Nystrom, U. Rempling, R. Gylltoft, K. 2011. A damage-plasticity model for the dynamic failure of concrete. 8th International confrence on structural dyanamics Leuven, Belgium.

Lubliner, J. Oliver, J. Onate, E. 1989. A plastic-damage model for concrete. International Journal of Solids and Structures, 25(3), pp. 299-326.

Lubliner, J. 2008. Plasticity Theory. U.S.A: Dover Publications.

Menetery, P. and Willam, K.J. 1995. Triaxial Failure Criterion for Concrete and its Generalization. ACI Structural Journal , Volume 92, pp. 311-318.

Rouquand, A. Pontinoli, C. and Mazars, J. 2007. Concrete structures under sever loading: a strategy to model the response for a large range of dynamic loads. Fracture Mechanics of Concrete and Concrete Structures: Proceeding of Fra MCoS 6.

Salari, M.R. Saeb, S. Willam, K.J. Patchet, S.J. Carrasco, R.C. 2004. A coupled elastoplastic damage model for geomaterials. Computer Methods in Applied Mechanics And Engineering.

Xotta, G. Beizaee, S. and Willam, K.J. 2014. Localization analysis of coupled plasticity and damage models.Computational Modelling of Comcrete Structures. PP 439-450 ed. London: Taylor and Francis Group.

Zhang, W. and Cai, Y. 2010. Continuum Damage Mechanics and Numerical Applications. China: Zhejhang University Press, Springer.

FINITE ELEMENT MODEL FOR THE TWO DIMENSIONAL FLOWS IN ALLUVIAL RIVERS

Engr. Oboshior Joel
Civil Engineering Department Ambrose Alli University Ekpoma Edo State Nigeria

Abstract
The basic equations governing physical and numerical studies of alluvial rivers enabled a prediction of inflow boundary conditions for the physical model. The exact mathematical models used for computing the unsteady flow in rivers constitute a difficult mathematical problem because of the nonlinear nature of the two simultaneous partial differential equations. Since numerical techniques are too time consuming, the two partial differential equations (St. Venant's equations), were simplified by omitting one of the two equations (momentum equation), or by omitting certain terms in this equation. The simplified equations were solved in several different ways, including the numerical integration by using manual successive approximation procedures. Numerical model was used to determine data such as pressure, velocity, flow depth and stream lines in the unsteady flow in an open channel mathematically governed by the Saint Venant's equation, using a four-point implicit finite difference scheme. A quasi two- dimensional "cell" model assumed that flood plain remained completely submerged only during the flood peak. The storage plotted versus the out flow discharge for inflow as (Q1, (115 m^3/s): out flow was (1570m^3/s) prepared for manual calculation, which can be very easily transformed for doing calculation by using the digital computer.
Key words: *Saint Venant's Equation: Cell Model: Finite difference scheme*

1. Introduction

1.1 Background to the Study

Alluvial rivers are rivers in which the bed and bank are considerately made up of sediments: self formed, consisting of channels, marked with eroded deposits, of sediments. They are based on the properties of the river banks, the amount, size and sediment present. Shaped by magnitude and frequency of the floods. [Shapiro, 2001]. The Technology soft ware's to measure, analyse, and investigate the water current is inadequate [Rudinger, 2001].

Mathematical modelling of fluid flow systems in rivers or storm systems, are governed by hydraulic equations; The solution by Saint Venant Equation for flood routing calculation is problematic for steady and unsteady flow simulation. [Cowling, 2002] flood estimation is important in creating water master plan; predict river bottle necks, and improve infrastructural development. [Vazsonyi .2003] Hydraulic modelling aids in the study of characteristics of unsteady flows in rivers,; changes in rivers, and roughness co-efficient; to match actual natural conditions. Models are categorized into ; Real system, Real system can be divided into, Mathematical Models, Empirical Models and Theoretical models. An empirical model may be considered as one that does not include general laws – it is mainly a representation of the data. These models are often called hydraulic-hydrologic models. Theoretical models are presumably the result of the most important general laws governing

the phenomena. physical models is preferred because it allows a real world situation; where such model help us to semilate systems of reservoirs; replicating flows and fluid transport processes in natural flow systems.[Doyle, et al 2003]. Most hydraulic engineers dealing with river hydraulics prefer the fixed grid methods; in other to solve the equation of motion at a fixed number of grid points in the (x, t) - plane. There are two basic types of fixed grid finite difference schemes: the explicit and the implicit scheme. In an explicit scheme, the equations are arranged so as to find the solution for one point at a time. In an implicit scheme, a group of advance points is solved by using simultaneous equations, which include the unknowns at all points in the group. To operate the finite differences using a fixed rectangular net in the (x, t) – plane. But, it is very important to notice; that the theory of characteristics, even it is not used directly, comes into play in deciding the relative values of (Δt) and (Δx) which will ensure convergence. As has been mentioned above, the x derivatives in the implicit schemes depends on the parameters of the flow regime in the "known" time (P), and the "unknown" time$(P + I)$ Equation 1

The implicit scheme is convenient for numeric computations of the unsteady phenomena with a long duration (flood waves). [Campbek, 1989]

The basis for a finite element method is similar to that for the two-dimensional model without the "inertial" terms. The model is composed of individual cells connected by river-type or weir-type links [Evans, 1988].

The equation used to donate the formula with regard to the direction of flow is q_i,

$$k = M_F \,.\, b.\sqrt{2g}\,(zk - 2i)^{3/2} \qquad Equation - - - 2$$

Were (M_f) is a discharge co-efficient

1.2 Finite El ement Model

The cells forming the model are arranged in a certain number of groups numbered in such a way that a cell belonging to a group (j) can only be lined to cells belonging to the same group (j), or the preceding group (j-1), or the following group (j + 1). This arrangement is illustrated by Fig.1

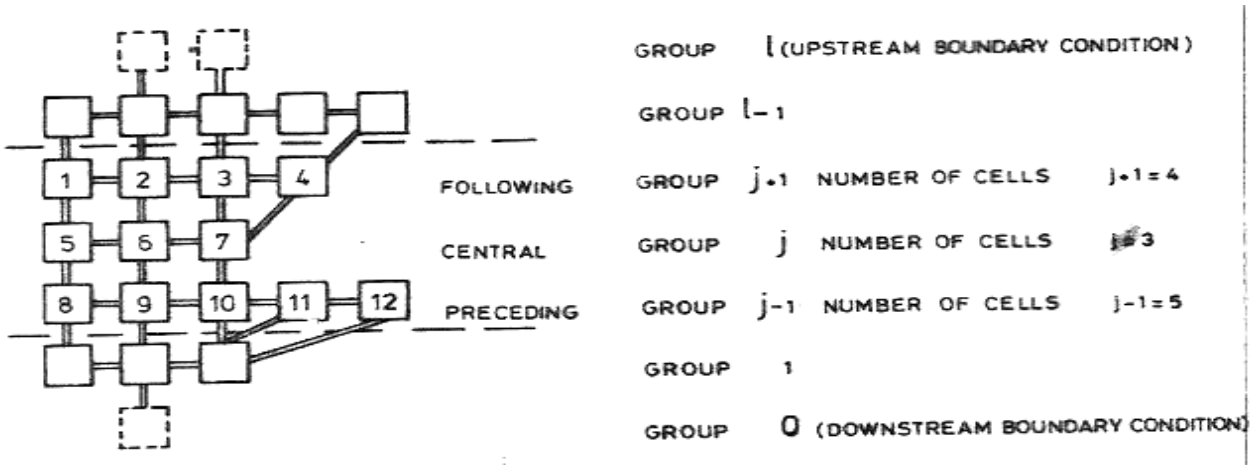

Figure 1 Scheme of cells

In Engineering, the Quasi two-dimensional and mathematical model, is described thus: it is assumed that the flood plains remains submerged, while separated by dikes, [Oboshior, 2018]. The slope of the water surface is defined for each cell ("I") by a horizontal level (Z_1) assumed at the centre of the cell. The continually equation is derived, were the volume $(\forall 1)$ of the water stored in cell (i) and k is a function of (Z_1) and (Zk).

The change in the volume of water stored in cell (i) during the time (Δt), is defined from the geometrical characteristics

$$\Delta \forall_i = \int_{zi(tn)}^{zi(tn+t)} A_1(Z_1)dzi \qquad Equation---3$$

From discharge conditions:

$$\Delta \forall_i = \sum_k \int_{t_n}^{t_n+\Delta t} Oi,k(Z_i\, i\, Z_k).dt \qquad Equation---4$$

Where: the suffix (k) donates the values of number of all cells neighbouring to cell (i). By averaging the integral over (Δt) and by comparing the volume increaments,

$\Delta Z \longrightarrow$ o $\quad \Delta t \longrightarrow$ o , and

$$A_I \frac{dzi}{dt} = \sum_k qi,k\,(z,;\, Zk) \qquad Equation---5$$

Computation of the steady non-uniform flow in rivers, is based on momentum equation of a gradually varied flow. The main objective of the computation is to determine the shape of the flow profile along the river.

2.0 Methods

Broadly classified there are three methods of computation; the graphical integration method; the direct-integration method and the step method: the development and procedure is characterized by a division of the channel into short river sub-reaches and by computations starting from the downstream and of the sub-reach up to the upstream end;

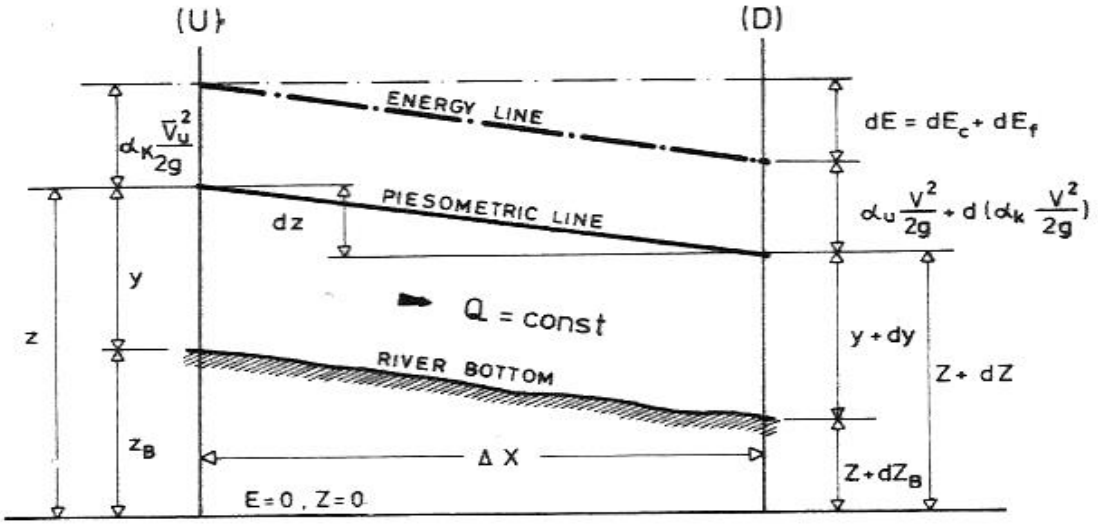

Figure 2 Sub-reach

Fig 2, illustrates a sub-reach of a length (x)

By equating the total heads at the two end sections "U" (upstream) and "D" (downstream), the following differential equation may be written:

$$-dz = dE_v + dE_1 + dE_f \qquad --- \text{Equation 6}$$

Where: (dE_v) — the loss of energy due to different velocities; (dE_1) — the eddy loss, which may be appreciable in non-prismatic channels: (dE_f) — the friction losses.

The terms on the right hand side of Eq. (90) can be written as:

$$\left.\begin{aligned} dE_v &= d\left(\frac{c\,v^2}{2g}\right) \\ dE_1 &= .d\left(\frac{\propto c\,v^2}{2g}\right) \\ dE_f &= \frac{v^2}{C^2 R}.dx \end{aligned}\right\} \qquad \text{Equation} --- 7$$

The eddy loss depends mainly on the velocity head change and may be expressed as part of it, where (ʒ) is a coefficient.

There is a lot of converse information about (ʒ). For example for Gradually converging and diverging reaches ʒ = 0 to 0.20, respectively. For abrupt expansions and contractions, (ʒ) is about 0.50. For converging reaches ʒ = 0, and for diverging reaches ʒ =-1.0!

After integration, the continuity equation for every cell is: $[\frac{dvi}{dt} = \sum_k Qi,k]$ the equation can be written in the following form.

$$Z = (1+ʒ).\left(\frac{\propto c\,v^2 D}{2g} - \frac{\propto c\,v^2 u}{2g}\right) + \frac{Q^2}{\bar{k}^2}\Delta x \qquad Equation --- 8$$

Where:

$$-\int_{Z_u}^{Z_D} dz \equiv \Delta Z$$

$$\frac{\propto c\, v^2 D}{2g}$$

$$\int (1+\xi).d\left(\frac{\propto c\, v^2}{2g}\right) \equiv (1+\xi).\left(\frac{\propto c.v^2 D}{2g} . \frac{\propto c.v^2 u}{2g}\right) \frac{\propto c.v^2 u}{2g}$$

$$\int_{x_U}^{x_D} \frac{v^2}{C^2 R} . dx \equiv \bar{s}_f$$

$(\propto_c)$ —the energy coefficient

The term $(\bar{s}_f)$ can be defined in different ways:

$$\bar{s}_f \equiv \frac{(Q)^2}{2} . \frac{1}{\left(A_u . R_u^{\,2/3}\right)^2} + \frac{1}{\left(A_D . R_D^{\,2/3}\right)^2} \qquad Equation---9$$

$$\bar{s}_f \equiv \frac{(Q)^2}{\left(\frac{2A_u A_D}{A_u + A_D}\right)^2 . \left(\frac{R_U + R_D}{2}\right)^{4/3}} \qquad Equation---10$$

$$\bar{s}_f \equiv \frac{(Q)^2}{\left(\frac{A_u + A_D}{2}\right)^2 . \left(\frac{A_U + A_D}{P_U + P_D}\right)^{4/3}} \qquad Equation---11$$

$$\bar{s}_f \equiv \frac{S_U + S_D}{2} \qquad Equation---12$$

The best results are obtained by using Eq (10) in Nigerian practice Eq (9) is used often.

If the eddy losses are small when compacted to the others, equation (8) can be written in the following form:

$$\Delta Z = Q^2 \left[\frac{\propto c}{2g}\left(\frac{1}{A_D^2} - \frac{1}{A_U^2}\right) + \frac{\Delta x}{\bar{K}^2}\right] \qquad Equation---13$$

Finally, if the velocity head change is small when compared to the friction loss, equation (8) is transformed to the Chezy formula, that is derived for a steady flow:

$$\Delta Z = \frac{Q^2}{\bar{K}^2} \Delta x = \frac{(nQ)^2}{(\overline{nk})^2} \Delta x \qquad Equation---14$$

If the river channel has several branches (see Fig. 2), the total discharge is defined by the following equation:

$$Q_T = \sum_{i=1}^{n} Q_i \qquad Equation - - - 15$$

Where: (Q_T) – total discharge; (i) – number of a branch.

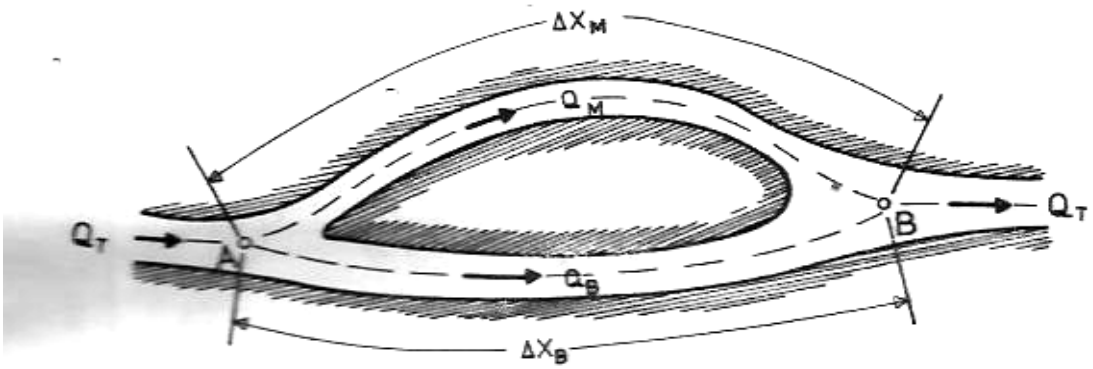

Figure 3 River Channel

Eq. (15) can be written in the derived from:

$$Q_T = Q_M + Q_B$$

Where: (Q_M) – the discharge in the main river channel;

(Q_B) – the discharge in a branch;

(Q_T) – the total discharge.

The difference between the water levels in points (A) and (B) is the same in the main channel and in the branch:

3.0 Results and Discussion

If the storage is plotted versus the outflow discharge, the resulting curve will generally take the form of a loop. As shown in Fig. (3), the storage for a given discharge on the rising (or falling) part of the flood wave will be greater than (or less than) the storage corresponding to the condition of a steady flow. The storage-outflow relationship for the condition of the steady flow is represented by the dashed curve, which is approximately at the average position of the two limbs of the loop, (dotted curve in Fig. 3).

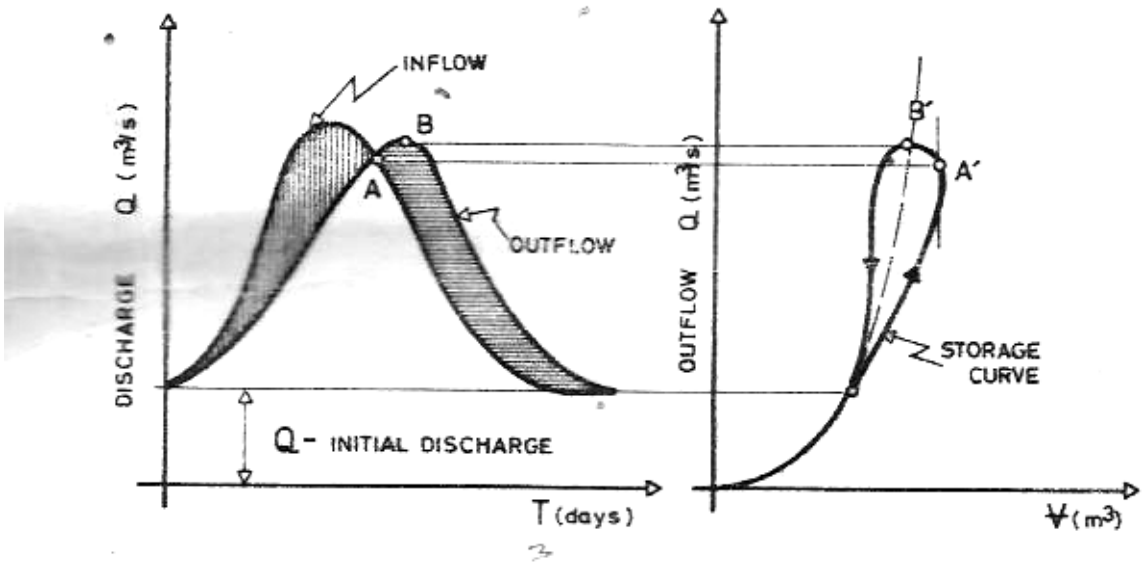

Figure 4

The loop can be very complex, and this depends upon the shape of the flood wave. Equation (5) can be written in the following form:

$$\bar{Q}_i - \bar{Q}_o = \frac{\Delta V}{\Delta t} \qquad \text{Equation} - - - 17$$

Where:

$\bar{Q}_i = \frac{Q_{i1}+Q_{i2}}{2}$ – average value of the inflow discharge in the time interval (Δt);

$\bar{Q}_o = \frac{Q_{o1}+Q_{o2}}{2}$ – average value of the outflow discharge in time interval (Δt);

$\Delta V = V_2(Q_{o2}) - V(Q_{o1})$ – the change of storage in the time interval (Δt), expressed as a function of the outflow discharge.

Eq (17) can be written in a derived form as:

$$\left(\frac{Q_{i1}+Q_{i2}}{2}\right) - \left(\frac{Q_{o1}+Q_{o2}}{2}\right) = \left(\frac{V_2(Q_{o2}) - V_1(Q_{o1})}{t}\right) \qquad Equation - - - 18$$

By using Eq. (18), function $F(Q_o)$ can be defined from the following equation:

$$\frac{V_2(Q_{o2})}{t} + \frac{Q_{o2}}{2} = \frac{Q_{i1}+Q_{i2}}{2} - \frac{Q_{o1}}{2} + \frac{V_1(Q_{o1})}{\Delta t} = F(Q_o)$$

As can be seen from Eq. (19) terms on the right side are known, so that the left side can be calculated easily, that means, the unknown outflow discharge (Q_2) also.

The procedure of computation is explained in Fig. (4) and Table (1)

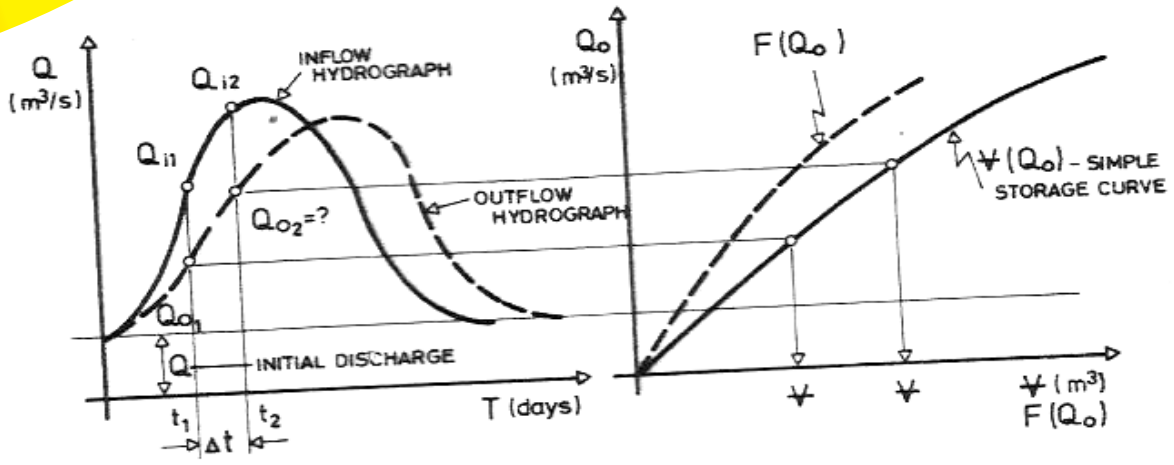

Figure 5 Out flow Discharge

Fig (4) computational process by the "quasi-steady" method

Table 1: Computational process by the "quasi-steady" Method

Date	ΔT	Inflow discharge			Outflow discharge			Outflow discharge
		Q_{i_1}	Q_{i_2}	$\bar{Q}_i$	$\frac{Q_{o_1}}{2}$	$\frac{(Q_{o_1})}{t}$	$F(Q_{o_1})$	Q_o
-	(days)	(m^3/s)			(m^3/s)			(m^3/s)
1.05.79	1	420	600	510	210	0	300	450
2.05.79	1	600	1150	875	225	60	710	710
3.05.79	1	1150	2000	1575	355	350	1570	1500

The above explained procedure is prepared for "manual" calculation. The method can be very easily transformed for doing calculation by using the digital computer.

4. Conclusion and Recommendation

4.1 Conclusion

The implicit system adapted in this model is a manual system that recognizes future computer operated method. This manual system simplified solutions using numerical equations 1-14; it was assumed that the river flood plains remained submerged, while separated by dikes. Sediments transport functions, moveable bed resistance posed numerical difficulty for strong hyperbolic equations, calibration, and validation of data arising from past researches is complex. The quasi calculation of inflow discharge and outflow discharge values are well tabulated.

4.2 Recommendations

This paper is recommending a computer research base work that can create a mathematical image or model of the physical process which will incorporate realistic assumptions and constraints. Information extracted in all the equations will be compared with physical evidence typically gained through experiments.

Reference

Campbek. R.G. (1989). "Theoretical Studies of Two Dimensional None Equillibrium Flow" *NASA Technical Report*.

Cowling, T.G, (2002). "A Digital Model for Stream Flow Routing by Convolution Methods". *US Geological Survey water Resources Investigations Report* 834162, P, 135.

Evans, J. S. (1988). *Method for Calculating effects of dissociation on flow variables in shock waves,*

Oboshior, J.(2018) "Mathematical Hydraulic Models of One- Dimensional Unsteady Flow in Rivers, *International Journal of Advanced Engineering Management and Science* (IJAEMS) http://dx:org/10.22161/ijacms. 4.2. vol2.

Rudingeri, G. (2001). *Linerized Theory of Steady High Speed Flow*; Cambridge University Press.

Vazsonyi, A, (2003). "Simulation of Unsteady Flow and Solute Transport in a Tidal River Network" *Engineering Computation"* 21(7/4), 222

EFFECT OF PALM OIL FUEL ASH (POFA) FINENESS ON THE FLOW AND STABILITY OF ASPHALTIC CONCRETE

Abdulmalik M. Maleka[1], Ramadhansyah P. Jaya[2], Ibrahim A. Adamu[2], Boaz T. David[4]

[1,&3]Department of Civil Engineering, Federal Polytechnic Bauchi, Bauchi State Nigeria
[2]Department Geotechnical and Transportation Engineering, University of Technology Malaysia (UTM), Johor Bahru, Malaysia
[4]Federal Road Maintenance Agency (FERMA), Jos, Plateau State, Nigeria

ABSTRACT

The amount and nature of filler (particles smaller than 75 μm) in an asphaltic concrete significantly affect its design and performance. The use of Palm oil fuel ash (POFA) as filler in asphaltic concrete has been studied with varying degrees of success. This study evaluates the effect of the fineness of POFA on the mechanical properties of asphaltic concrete. Using 4 different categories of POFA fineness (based on 30min, 60min, 90min and 120min of grinding with Los Angeles Abrasion Value (LAAV) machine), a number of trial mixes were prepared using the Marshal Mix design procedure with 5% POFA to arrive at asphalt concrete mixtures that fulfill the Marshal criteria. The effects of each POFA fineness category on the stability, flow and stiffness of asphaltic concrete mixtures at their respective optimum binder content were evaluated. The results show that Marshall stability, flow and stiffness generally improve when POFA is grinded than the control, but after some period of grinding (peak of the curve), the values diminished. Hence, grinding POFA improves the stability and stiffness of asphaltic concrete by 25% and 20% respectively. Grinding POFA for up to 60 minutes gives the optimum improvement of the properties of asphaltic concrete mixes considered in this study.

Keywords: Palm oil fuel ash (POFA); Filler; Flow; Stability; Asphaltic Concrete

1. INTRODUCTION

The history of road construction dated back to the Roman roads of the 18th centuries. However, despite this long history and hence the vast experience of road construction, engineers are still facing challenges of road failures. These pavement failures represent serious economic lost to countries all over the world, Malaysia is not an exception. Malaysia is witnessing rapid economic development in recent years, and this has placed high performance demand on its highway infrastructure. Evidence of early pavement failures has been widely reported on Malaysian roads due to increased axle loading among other factors. (Kordi, 2010). This trend has pushed the conventional design methods and construction materials to the edge. Thus the need for sustainable construction materials cannot be overemphasize.

Researchers worldwide try to develop better composites, affordable and more resistant, road construction materials that can sustain the rapid growth in axle loading. Many different, and sometimes conflicting, performance demands are placed upon the asphalt mixtures and this makes it a complex material. Normally, at room temperature bitumen is soft with a density of 1 g/cm^3, but at low temperature it becomes brittle and at high temperature it flows like a viscous liquid. Aging, which occurs in asphalt roadway pavements during construction and service life,

affect the rheological properties of bitumen. Rheology simply means the flow of fluids and deformation of solids under stress and strain (Yero and Hainin, 2012).

Thus, the design of asphalt concrete mixes is largely a matter of selecting and proportioning the ingredient materials to optimize all desired properties in the finished paved road. Amongst the components of the asphaltic concrete mixes is the filler, which is a fine material passing the No. 200 sieve. Better understanding of the role of fillers on the performance of asphalt mixtures is important in paving material research.

Fillers have only been thought to fill voids in the aggregate. However, studies indicate that the role of fillers in asphalt mixture performance is more than filling voids depending on the type used. Many studies have been carried out on effects of fillers on the behavior of asphalt mix (Asi and Assa'ad, 2005; Karasahin and Terzi, 2007; Mehari, 2007; Hafeez and Kamal, 2009; Muniandy and Aburkaba 2011). Different filler materials may have different mechanical properties in the asphalt mixture. However, a thorough understanding of the effect of fine particulate fillers in asphalt binders and mixes has not been reached.

Malaysia is one of the leading producers of crude palm oil with around 41% of the total world supply in years 2009–2010. The by-product of Palm oil production has been disposed as waste thus causing environmental problems and health hazards. Some of the waste materials with high fuel value, such as palm oil husks and shells, can be reused as fuel to produce steam for generating electricity, which is required for extracting crude palm oil. After combustion, about 5% of palm oil fuel ash (POFA) or boiler ash is produced. POFA when properly processed has shown to be a good construction material in concrete and mortar, Altwair et al. (2011).

A study by Borhan et al (2010), reports that the replacement of 5% mineral filler by POFA improved the performance of asphaltic concrete in terms of resilient modulus, stiffness and fatigue properties. In another study, Ahmad et al (2012) found that ACW20 design can apply POFA as filler in particular percentage.

The aim of this study is to evaluate the effect of POFA particle size on the properties of asphaltic concrete through the following objectives:

i. To investigate the effect of different particle sized POFA on the stability, flow, and stiffness of asphaltic concrete mix.

ii. To determine the optimum fineness of POFA for asphaltic concrete.

2. MATERIALS AND METHODS

2.1 Materials

Asphalt bitumen used in this study was 80/100 penetration grade. Since the performance of filler is of concern here, commonly used asphalt cement was selected. The aggregate used in this study was granite stone obtained from Malaysia Rock Product Sdn Berhad (MRP) at Ulu Choh, Pulai, Johor Bahru, Malaysia. The crushed stones (coarse and fine) obtained from the quarry were blended to meet the gradation requirement of AC14 as recommended by the Malaysia Ministry of Public Works (JKR) gradation for a heavy traffic wearing course, as shown in Table 1 Sieve analysis was conducted on the collected samples and the selected aggregate sizes all fall within the range specified as shown in figure 1.

Table 1 Gradation Limits for Asphaltic Concrete AC14 (JKR 2008)

Sieve size (mm)	% passing by weight	Selected gradation
20	100	100
14	90-100	95
10	76-86	81
5	50-62	56
3.35	40-54	47
1.18	18-34	26
0.425	12-24	18
0.15	6-14	10
0.075	4-8	6

Two types of filler materials were used in the study, Palm Oil Fuel Ash (POFA) and Ordinary Portland Cement (OPC). POFA used in this study was sieved through 75µm sieve to ensure that it satisfied ASTM filler material definition of 70%-100% passing 75µm sieve. The physical and chemical analyses of POFA is presented in Table 2.

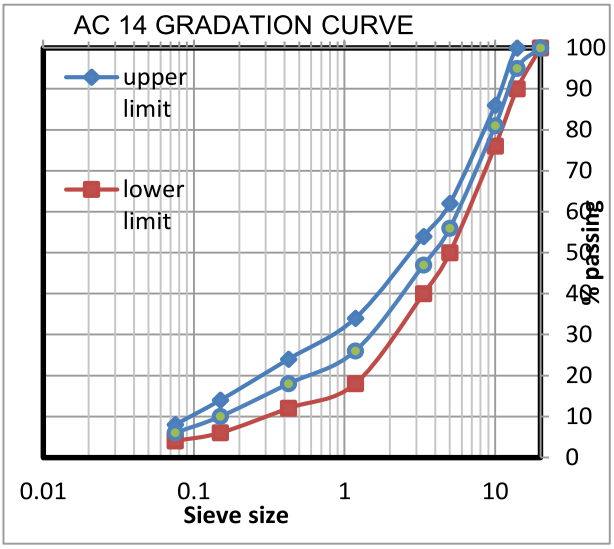

Figure 1: Shows gradation envelope limits for AC14

Table 2: Physical and chemical properties of POFA

Property	Specific gravity	2.22
Chemical composition (Percentage)		
Silicon dioxide		71.20
Carbondioxide		0.10
Ferric oxide		7.12
Calcium oxide		4.37
Magnesium oxide		1.95
Sulphur trioxide		0.89
Potassium oxide		5.59
Loss on ignition		8.78

(Source; Galau and Ismail, 2010)

The POFA was oven-dried before sieving through 75µm sieve. Thereafter; it was grounded for four (4) different times duration, 30, 60, 90 and 120minutes to have four different particle size proportions using Los-Angeles Abrasion Value equipment with 10 steel rods. After grinding, the POFA was sieved using 40µm sieve to check the effect of grinding. Table 3 shows the percentage of POFA passing 40µm sieve after grinding for 30, 60, 90 and 120minutes.

Table.3: Percentage of POFA passing 40µm

POFA Grinding Period (min)	Percentage Passing 40µm sieve (%)
30	50.9
60	54.7
90	64.7
120	69.5

2.2 Methodology

2.2.1 Sample Preparation

To achieve the objectives of this study, 72 samples POFA modified asphalt concrete were prepared using 5% POFA as an additive of the mineral filler and 1% OPC. The samples were used to establish the optimum binder content (OBC) for the four different particle size proportions through the Marshal procedure with 4-6.5% bitumen content.

2.2.2 Laboratory Tests

Preliminary tests

All laboratory tests were conducted in accordance with ASTM specifications. Preliminary tests carried out include specific gravity of aggregate, which provides important information for designing Hot Mix Asphalt (HMA) because it is used to calculate Void in Total Mix (VTM) and Void Fill with Bitumen (VFB). ASTM C127-12 standard for determination of specific gravity of coarse aggregate was adopted in this study. Similarly, ASTM C 128-12 was adopted for determining the specific gravity of the fine aggregate. The effective specific gravity cannot be measured directly, so it was calculated from the theoretical maximum density. The theoretical maximum density was determined in accordance with ASTM D2041/D2041M – 11. The specific gravity and penetration grade of binder was adopted based on the suppliers' measurements, likewise for POFA and OPC.

Sieve analysis was carried out according to ASTM C136 – 06, for the selection of AC14 aggregates based on JKR 2008 recommendation.

Marshall Mix Design

Marshall Stability and Flow tests were carried out in order to find the optimum binder content (OBC) of the mixes. The Marshall Mix design procedure (ASTM D6927 - 06) currently used in Malaysia for asphalt concrete mix design to determine the optimum binder content was adopted.

3. RESULTS AND DISCUSSION

3.1 Preliminary Tests

The results of specific gravity test conducted on both coarse and fine aggregates a
were presented in table 4.

.

Table 4: Physical Properties of Materials

S/N	PROPERTY	VALUE (g/cm^3)
1.	Bulk Specific Gravity of Aggregate	2.60
2.	Effective Specific Gravity of Aggregate	2.63
3.	Specific Gravity of Bitumen	1.03
4.	Specific Gravity of POFA	2.22

3.2 Marshall Characteristics

The 4-6.5% asphalt content range was used to determine the optimum asphalt content for the five (5) categories of POFA fineness considered in this study. Parameters used in arriving at the OBC are Stability, Flow, VTM and VFB in accordance with JKR 2008 AC 14 for wearing coarse recommendations. Table 5 presents the OBC obtained.

Table 5: OBC for each mix

S/N	TYPE OF MIX	OBC (%)
1.	No Grinding (Control)	6.2
2.	30 Minutes Grinding	6.0
3.	60 Minutes Grinding	6.0
4.	90 Minutes Grinding	5.6
5.	120 Minutes Grinding	5.5

It was observed that based on the OBC, there is probably no significant difference between 30 minutes and 60 minutes grinding. Similarly, not much difference between 90 minutes and 120 minutes grinding were observed.

Table 6: Marshall Mix Design Characteristics at OBC

MASHALL PARAMETERS	TYPE OF MIX					JKR 2008	RESULT
	No	30	60	90	120		

	Grinding	min.	min.	min.	min.		
Stability (N)	13783	15206	15696	16088	14617	>8000	PASS
Flow (mm)	3.6	3.7	3.6	3.55	3.6	2.0-4.0	PASS
Stiffness (N/mm)	3728	4415	4415	4120	4120	>2000	PASS
VTM (%)	7	6	5	4.8	4.1	3.0-5.0	FAIL
VFB (%)	65	70	75	70	70	70-80	FAIL

The JKR recommendation for asphalt content range is 4 – 6% for AC 14 (wearing course), however, 4 – 6.5% was used in this study because at 6% asphalt content, no clear peak was observed on the density curve for all mix types.

Marshall Characteristics; stability, flow, stiffness, VTM and VFB were measured at OBC for all the mixes and compared with JKR recommendation for AC 14 as presented in table 6.

It was observed that VTM for the control and 30 minutes grinding mixes failed to meet JKR recommendation of 3.0 -5.0% for wearing course but it met the recommendation for binder course which is 3.0 – 7.0%. Similarly, VFB for the control mix failed. However, the JKR 2008 specifications adopted in this study is for AC 14 using conventional filler material not POFA. JKR therefore allow for adjustment of the specifications when special mix is involved that is not covered by the manual based on local experience.

Figures 2 to 6 shows how Marshall Parameters; stability, flow, stiffness, VTM and VFB vary with the particle size of POFA based on period of grinding.

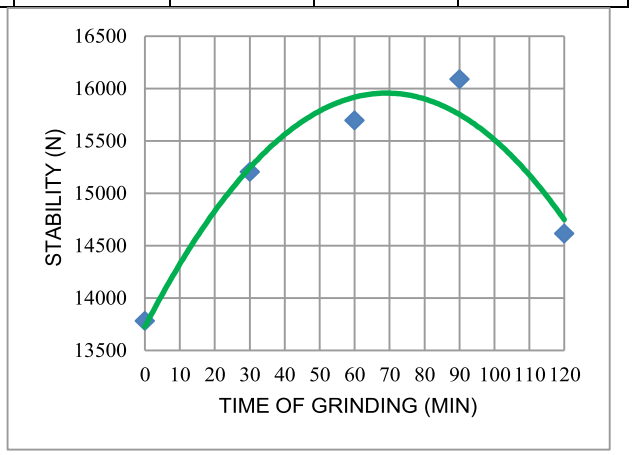

Figure 2: Variation of Stability with POFA fineness

Figure 2 shows a parabolic curve depicting how the stability of asphaltic concrete (AC 14) varies with increasing fineness of POFA. From the curve, POFA fineness at 70 minutes of grinding gives the best stability compared with the control. Hence, amongst the four fineness category considered in this study, Sample with 60 minutes of grinding gives best stability result. This can be attributed to the fact

that filler in asphaltic concrete stiffen the mix hence makes it stable. As the fineness increases, the stiffness as well as the stability of the mix increases. When the fineness continues to increase, the mastic formed by the combination of the filler and binder will begin to flow, hence the stability of the mix reduced.

According to JKR 2008, the best value of flow for AC 14 is 3mm which is the mid-point of 2 - 4mm recommended. From figure 3, the closest flow to 3mm is 3.55mm which occur at 90 minutes

of grinding. After which the flow begins to rise with increase in fineness.

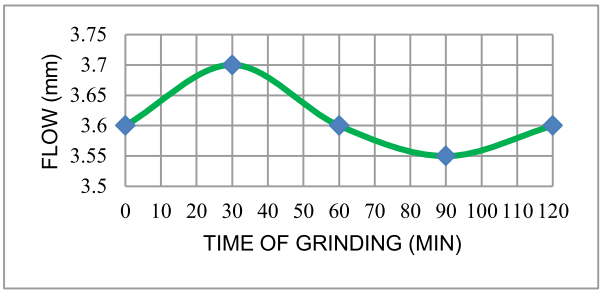

Figure 3: Variation of Flow with POFA fineness

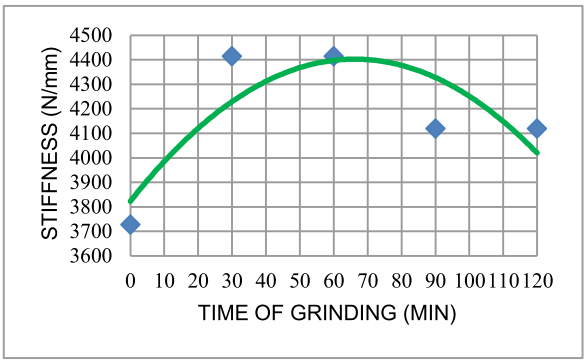

Figure 4: Variation of Stiffness with POFA fineness

Figure 4 shows a parabolic curve depicting how the stiffness of asphaltic concrete (AC 14) varies with increasing fineness of POFA. From the curve, POFA fineness at 60 minutes of grinding gives the best stiffness compared with the control. Hence the optimum POFA fineness that gives best stiffness result is at 60 minutes of grinding. . This is also due to the fact that as filler fineness increases, the stiffness of the mix increases. When the fineness continues to increase, the mastic formed by the combination of the filler and binder will begin to flow, hence the stiffness of the mix reduced.

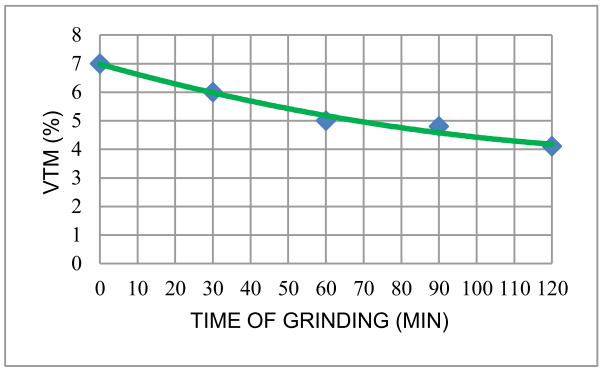

Figure 5: Variation of VTM with POFA fineness

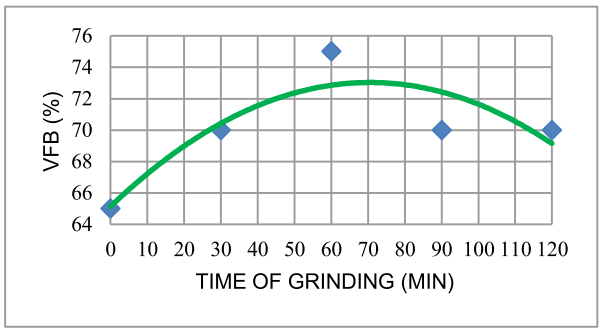

Figure 6: Variation of VFB with POFA fineness

Figure 5 shows a negative linear relationship between POFA fineness and VTM. This implies that the volume of voids in the total mix decreases with increasing POFA fineness. This may be attributed to the fact that as POFA particles is becoming smaller it filled up more void spaces in the mix.

Figure 6 shows that at 60 minutes of grinding, volume of void filled with bitumen is best. Thereafter, increase in POFA fineness result to lower VFB. This may be attributed to the fact that as POFA particles is becoming smaller; it takes over some void spaces that may have being filled by bitumen.

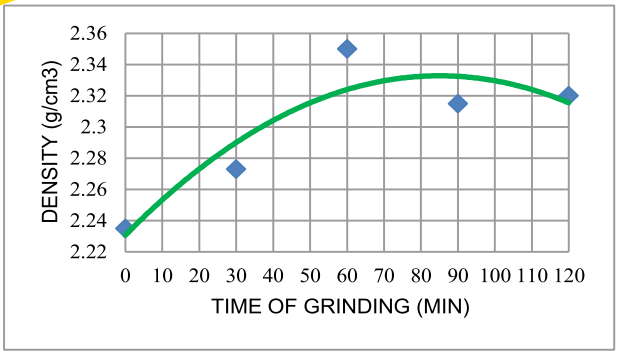

Figure 7: Variation of Density with POFA fineness

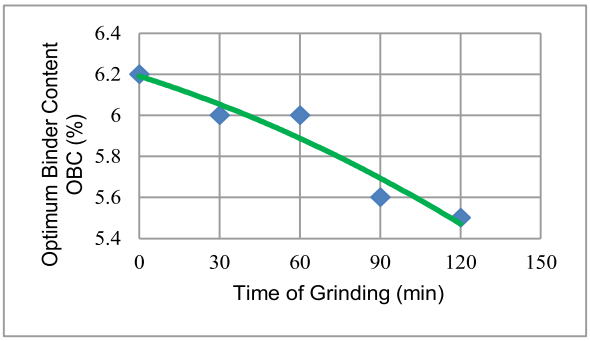

Figure 8: Variation of OBC with POFA fineness

Almost all the curves with the exception of VTM and OBC show a parabolic curve with the peak of the curve representing the best POFA fineness. Figure 7 shows a parabolic relationship between density and POFA fineness and Figure 8 shows that finer the POFA particles the less the quantity of bitumen required. Table 7 presents a summary of the POFA fineness (time of grinding) that gives the best Marshall parameters.

Table 7: Optimum POFA Fineness

S/N	MARSHALL PARAMETERS	POFA FINENESS (MIN. OF GRINDING)
1.	STABILITY (N)	60
2.	FLOW (mm)	90
3.	STIFFNESS (N/mm)	60
4.	VFB	60
5.	DENSITY	85

4. CONCLUSION

For the mixtures evaluated in this study, the following conclusions are derived.

- Marshall Stability, flow and stiffness values were found to be generally better when POFA is grinded than the control, but after some period of grinding, the values of stability and stiffness reduced. Hence, grinding POFA to some extent improves the stability, flow and stiffness of asphaltic concrete.
- Grinding POFA for up to 60 minutes gives the optimum improvements of the properties of asphaltic concrete mixes considered in this study.

5. REFERENCES

Ahmad J., Yunus K. N., Kamaruddin N. H. and Zainorabi din A. (2012) The practical use of palm oil fuel ash as a filler in asphalt pavement. Faculty of Civil Engi neering, U.T.H.M, BatuPahat, Johor

Altwair M. N., Johari M. A. M. and Hashim S. F. S. (2011) Strength Activity Index and Microstructural Charac teristics of Treated Palm Oil Fuel Ash International Journal of Civil & Environmental Engineering IJ CEE-IJENS Vol: 11 No: 05

American Society for Testing and Material,

ASTM C127-12 (2012). Test Method of Specific Gravity and Absorption of Course Aggregate. Philadelphia, USA,
American Society for Testing and Material, ASTM C128-12 (2012) Test Method of Specific Gravity and Absorption of Fine Aggregate. Philadelphia, USA,.
American Society for Testing and Material, ASTM D2041/D2041M-11 (2011). Test Method of Theoreti cal Maximum specific Gravity and Density of Bitu minous Paving Mixtures. Philadelphia, USA.
American Society for Testing and Material, ASTM C136-06 (2006). Test Method of Sieve Analysis of Fine and Coarse Aggregates. Philadelphia, USA,
American Society for Testing and Material, ASTM D6927-06 (2006). Test Method of Marshall Stability and Flow of Bituminous Mixtures. Philadelphia, USA,
American Society for Testing and Material, ASTM D6926-10 (2010). Test Method of Preparation of Bituminous Specimens Using Marshall Apparatus. Philadelphia, USA,
Asi, I. and A. Assa'ad, 2005. Effect of Jordanian oil shale fly ash on asphalt mixes. Journal of Materials in Civil Engineering, 17: 553-559.
Borhan M. N., Ismail A. and Rahmat R. A. (2010) Eval uation of Palm Oil Fuel Ash (POFA) on Asphalt Mixtures. Australian Journal of Basic and Applied Sciences, 4(10): 5456-5463, 2010 ISSN 1991-8178 ,INSInet Publication.
Galau, D., & Ismail, M. (2010). Characterization of Palm Oil Fuel Ash (POFA) from Different Mill as Cement Replacement Material (Doctoral dissertation, Thesis, Faculty of Civil Engineering, UniversitiTeknologi Malaysia, Johor, Malaysia).
HafeezI. and Kamal M. A. (2009) Effects of Mineral Filler to Polymer Modified Bitumen Ratio onthe Design Properties of Hot Mix Asphalt and its Performance. Mehran University Research Journal of Engineering & Technology, Volume 29,No. 4, October, 2010 [ISSN 0254-7821]
Jabatan Kerja Raya (2008), Standard specification for Road Works. Kula Lumpur, (JKR/SPJ/rev2008).
Karasahin, M. and S. Terzi, 2007.Evaluation of marble waste dust in the mixture of asphaltic concrete.Constr and Build Mater., 21: 616-620.
Kordi, N. E., Endut, I. R., & Baharom, B. (2010)Types of Damages on Flexible Pavement For Malaysian Fed eral Road. Proceeding of Malaysian Universities Transportation Research Forum and Conferences 2010(MUTRFC2010), 21 December 2010, UniversitiTenagaNasional. ISBN 978-967-5770-08-1
Mehari B. Z. (2007) Effect of Different Types of Filler Materials on Characteristics of Hot-Mix-Asphalt Concrete. Master Thesis Submitted to School of Graduate Studies of Addis Ababa University.
Muniandy R. andAburkaba E. E. (2011).The effect of type and particle size of industrial wastes filler on Indirect Tensile Stiffnessand Fatigue performance of Stone Mastic Asphalt Mixtures.Australian Journal of Basic and Applied Sciences, 5(11): 297-308, 2011ISSN 1991-8178.
Yero, S. A. and Hainin, M. R. (2012) Evaluation Of Bitumen Properties Modified With additive IJRRAS 13 (1) October 2012.

Nigerian Institution of Civil Engineers

Sustaining the World's Infrastructure....

A Division of The Nigerian Society of Engineers

Announces her

20th INTERNATIONAL CIVIL ENGINEERING CONFERENCE AND AGM, 2022

THEME:

SUSTAINABLE CIVIL INFRASTRUCTURE DEVELOPMENT IN A CHALLENGING ECONOMY

- Technical Sessions
- Industrial Visits
- Cultural Displays
- Annual General Meeting
- National Chairmans Cocktail
- Election of Executive Officers
- Celebration of Achievers
- Exhibitions
- Annual Dinner
- Spouses Programs
- Young Engineers/Student Activities

DATE:

12th to 14th OCTOBER, 2022

NICE NATIONAL SECRETARIAT

Labour House, 8th Floor, Central Business District Abuja Nigeria.

CONFERENCE ENQUIRES:

Engr. Dr. Robbie James Owivry, FNICE
Chairman, Central Planning Committee
08033230754

Engr Olawale Bolarinwa, MNICE
Chairman, Local Organising
08022252921

Olayemi Ojofeitimi
Public Relations Officer
08023388223

Mr Bright Ochiabuto
Admin Officer
07062070193

Engr David Tope Boaz, FNICE
Executive Secretary
08037154335

VENUE: D'Podium, 31B, Aromire Avenue, Off Adeniyi Jones, Ikeja, Lagos , Nigeria

https://conference2022.nicelagos.org.ng/